2009-07-02

Cross-Correlation-Based Texture Analysis Using Kinematically Simulated EBSD Patterns

Joshua Peter Kacher
Brigham Young University - Provo

CROSS-CORRELATION-BASED TEXTURE ANALYSIS USING KINEMATICALLY SIMULATED EBSD PATTERNS

by

Josh Kacher

A thesis submitted to the faculty of

Brigham Young University

in partial fulfillment of the requirements for the degree of

Master of Science

Department of Mechanical Engineering

Brigham Young University

August 2009

BRIGHAM YOUNG UNIVERSITY

GRADUATE COMMITTEE APPROVAL

of a thesis submitted by

Josh Kacher

This thesis has been read by each member of the following graduate committee and by majority vote has been found to be satisfactory.

Date	Brent L. Adams, Chair
Date	David T. Fullwood
Date	Branton J. Campbell

BRIGHAM YOUNG UNIVERSITY

As chair of the candidate's graduate committee, I have read the thesis of Josh Kacher in its final form and have found that (1) its format, citations, and bibliographical style are consistent and acceptable and fulfill university and department style requirements; (2) its illustrative materials including figures, tables, and charts are in place; and (3) the final manuscript is satisfactory to the graduate committee and is ready for submission to the university library.

Date

Brent L. Adams
Chair, Graduate Committee

Accepted for the Department

Larry L. Howell
Graduate Coordinator

Accepted for the College

Alan R. Parkinson
Dean, Ira A. Fulton College of Engineering and Technology

ABSTRACT

CROSS-CORRELATION-BASED TEXTURE ANALYSIS USING KINEMATICALLY SIMULATED EBSD PATTERNS

Josh Kacher

Department of Mechanical Engineering

Master of Science

The development and example applications of a new EBSD-based texture analysis system are presented. This new system uses the cross-correlation function to compare two EBSD patterns at a number of corresponding regions in each pattern to calculate the deformation gradient tensor. Bragg's Law-based simulated EBSD patterns are used as reference patterns in the cross-correlation method to enable the measurements of absolute elastic strain and lattice orientation at discrete points in a crystalline sample.

The resolution limits of this new method are explored using a variety of computational and physical experiments. The simulated pattern method is estimated to be able to measure lattice orientations to within +/-0.02° and elastic strains to within $+/-3.6x10^{-4}$ for small strains and $+/-1x10^{-3}$ for large strains.

Two example applications are demonstrated. The first demonstration is estimating the dislocation density in a 5.5% compressed Mg-based AZ91 alloy. Nye's and Kröner's

formulations are used to estimate the dislocation density. Comparisons are made with traditional OIM measurements and it is found that the simulated pattern method offers an order of magnitude improvement in dislocation density estimations over OIM.

The second demonstration is tetragonality measurements of HSLA 65 steel along the weld line of a friction stir welded plate. Accurate tetragonality measurements in the bainite phase of the steel can be made using information from the diagonal components of the elastic strain tensor. The measured tetragonality can be related to the concentration of interstitial carbon atoms in the iron lattice to find the carbon distribution in the sample.

From these experiments, it is demonstrated that the simulated pattern method presents a new and powerful methodology for texture analysis that exhibits both ease of use and access to high resolution orientation and elastic strain data.

ACKNOWLEDGMENTS

The majority of my thanks goes to my committee chair Dr. Brent Adams for the guidance and time that he has devoted to me, and the excitement that he has helped to instill in me for my research. Without him, I likely never would have gotten into the materials world. I would also like to thank the other members of my committee, Dr. David Fullwood and Dr Branton Campbell.

Colin Landon deserves much of my thanks for writing the original version of the simulated pattern code and starting us on this path of high resolution EBSD-based texture analysis. Also, Dan Seegmiller and Stuart Rogers deserve thanks for getting the custom SEM stage built just in time for me to get my final results. For scintillating conversation and help when I got stuck, I would like to thank other members of my lab: Jay Basinger, C.J. Gardner, Scott Lemmon, Ribeka Takahashi, Sadegh Ahmadi, Kim Stevens, and Oliver Johnson.

I would also like to thank for everything that I am and have accomplished so far in life my parents, Larry and Pauline Kacher.

Finally I would like to acknowledge ARO for their financial support.

TABLE OF CONTENTS

LIST OF TABLES

LIST OF FIGURES

1 Introduction

The first fully automated electron backscatter diffraction (EBSD) indexing system, known as orientation imaging microscopy (OIM), was introduced in 1991 [1]. Since then, OIM has become a key tool in the study and characterization of metals and ceramics. By applying a Hough transform to EBSD patterns, Kikuchi bands are detected and indexed from a lookup table. In this manner, statistically significant datasets on the crystal orientation of a material can be collected in relatively short amounts of time. OIM has become a standard tool in many laboratories around the world with applications ranging from the study of semiconductors to microstructural optimization of components of mechanical devices.

The largest advancements in OIM and EBSD-based texture analysis have been in hardware with increased camera speeds and improved convergence of the electron beam to increase spatial resolution. Current camera and indexing speeds are now as high as 450 patterns per second. Past trends suggest that the camera speed will continue to increase as new cameras are developed and computational power for pattern indexing increases [2]. The spatial resolution is limited by the interaction volume of the electron beam with the sample and the software's ability to deconvolve mixed EBSD patterns at grain boundaries. The interaction volume of the electron beams limits the ability of OIM to reliably characterize materials with a grain size smaller than ~100 nm [3-6]. Another area

of advancement in OIM is the relatively recent advent of three dimensional OIM [7, 8]. This has been made feasible and practical by the coupling of a focused ion beam (FIB) with the scanning electron microscope (SEM) system. High precision serial sectioning can be carried out using the FIB and three dimensional orientation maps can be constructed from the data obtained from each section.

While OIM related hardware has continued to improve, there has been little change in the basic methodology of OIM. Multiple studies have reported the angular resolution of Hough based analysis methods to 0.5-1° [9]. The resolution limitations of Hough based methods are insufficient for meaningful elastic strain measurements. These two limitations (angular resolution and elastic strain) have motivated the search for new, high resolution methods of EBSD-based texture analysis.

A cross-correlation-based orientation and strain measurement system introduced by Troost et. al. [10] and refined by Wilkinson et. al [11, 12] has been shown to achieve orientation resolution to 0.006° and, when boundary conditions are taken into account, measures all nine components of the elastic strain tensor to $1x10^{-4}$. In brief, this new method uses direct comparisons of collected patterns by way of the cross-correlation function applied at a number of regions on the pattern. Using this comparison technique the elastic strain gradient and rotation tensors can be measured at each point from which an EBSD pattern is collected. In order to measure the absolute elastic strain and orientation at each point, a reference pattern must be obtained from a precisely known lattice state. In practice, such patterns exist only in limited situations. The cross-correlation method provides an important base for the method later presented, and so will be discussed in more detail in a subsequent section.

Because of its dependence on a reference pattern, the cross-correlation method has thus far been limited in its use to two main applications. The first use is with samples that have (relatively) strain free portions from which a reference pattern can be collected. In the first demonstration of the use of the cross-correlation method, Troost et al. measured the elastic strains across the interface of epitaxial silicon germanium layers. Wilkinson et al. have also demonstrated in multiple instances the cross-correlation method's ability to facilitate high resolution studies of elastic strain and rotation behavior across silicon germanium epilayers [13, 14]. Villert et al. also applied this method to characterizing the interface between silicon germanium layers along with measuring the strain distributions across a silicon sample subject to four-point bending [15]. In each case, a reference pattern was collected far from the interface. The second use is when only gradient information is needed. This is the case when measuring curvatures or dislocation densities of a material. Wilkinson et al. demonstrated the ability to measure variations in dislocation densities leading up to a fatigue crack tip in a nickel based super alloy [11]. Landon et al. were also able to demonstrate the cross-correlation method's usefulness in characterizing the dislocation state of a material using a well annealed polycrystalline nickel sample in the interior of a single grain [16]. Gradient information can also be important when the aim is to study elastic strain concentrations and the magnitude of misorientations in a sample. This use was demonstrated by Miyamoto et al. by investigating the local strain fields in the austenite phase caused by shape strain accommodation associated with the formation of martensite [17].

Simulated EBSD reference patterns provide an attractive possibility to maintain the increased angular resolution and access to elastic strain information that the cross-

correlation method provides while still keeping the more general applicability of traditional OIM [18]. Winkelmann has produced stunning results with high fidelity dynamical simulations of EBSD patterns [19, 20]. These simulations generally use Bloch wave theory to accurately predict the placement of Kikuchi bands as well as intensity variations over the EBSD pattern. Dynamical simulations are, however, extremely computationally expensive (a single pattern simulation can take anywhere from hours to days). With current computational capabilities, it is impractical to dynamically simulate reference patterns for the cross-correlation method. Instead, simple Bragg's Law or kinematical simulations have been investigated as potential reference patterns with the cross-correlation method [21]. Although these simulations do not accurately predict the variations in intensity over a pattern, they do accurately predict the Kikuchi band placements and widths. Since the cross-correlation method relies on measurements of shifts in Kikuchi bands for strain and orientation measurements, it is proposed that Bragg's law-based simulations provide sufficient detail to be useful as reference patterns.

There are two fundamental questions upon which the feasibility of using Bragg's Law-based simulations as reference patterns hangs. First, will the cross-correlation analysis of a measured and simulated pattern return appropriate shifts, and second, are kinematical simulations sufficiently accurate to make meaningful measurements. A series of verification tests in chapter 3 shows that by iteratively generating the simple patterns at each calculated deformation state of a measured pattern and then repeating the calculation with the new simulation, a high resolution result—approaching the levels of the standard cross-correlation method—is rapidly found by convergence. Each deformation state is calculated with respect to a fixed initial state. In this way, the benefits of the cross-

correlation method are kept while the limitations associated with needing a strain free reference pattern are eliminated.

Chapters 4 and 5 of this paper describe example applications of the simulated pattern method. In chapter 4 the method's usefulness in estimating dislocation densities is demonstrated. In chapter 5 it is shown that simulated patterns can be used to detect and measure the crystal lattice tetragonalities that arise in different phases of friction stir welded steel due to interstitial carbon atoms.

2 Development of the Simulated Pattern Method

2.1 Cross-correlation analysis algorithm

The approach developed by Troost and Wilkinson forms the underpinnings of the simulated pattern method to be introduced, so its fundamentals are briefly described.

Many regions of interest (ROIs) (normally 10-20) are spread uniformly around a reference EBSD pattern (see figure 2-2 for visualization). For a 1000x1000 pixel image, these regions are usually selected to be of size 256x256 pixels. Ideally, the orientation and lattice strain of the reference pattern are known. In reality the lattice state can be known only to the precision of traditional methods informed by knowledge of the material in question. ROIs in corresponding positions are placed in a different collected pattern of unknown character. The cross-correlation function is then used to determine how the corresponding ROIs in the two patterns would need to be shifted in order to align similar features with each other. The cross-correlations are closely related to the convolution of two functions and can be calculated efficiently in the Fourier domain by the following equation. ($\Im\{...\}$ indicates the Fourier transform, *conj*(…) the complex conjugate, and * indicates element-wise multiplication of two matrices).

$$C = \Im^{-1}\left\{\Im\{f\} * conj\left(\Im\{g\}\right)\right\} \tag{1}$$

The resulting image, *C*, shows intensity peaks related to shifts that cause similar features to be aligned. The peak intensity in *C* is located at a position described by the vector $\vec{q}$ measured from the center of the image (i.e. if the peak appears at the center then $\vec{q}$ would have components [0,0], if the peak appears one pixel to the right of and one pixel down from the center then $\vec{q}$ would have components [1,-1]). The vector $\vec{q}$ describes how (on average over the ROI) features contained in the selected ROI shift when compared to other patterns that also contain the feature. Local interpolation schemes over a number of ROIs allow the tracking of a feature shift down to 1/20th of a pixel. Although this shift is the average of all features in the region, it approximates the shift of the pattern direction, $\hat{r}$, found at the center of the ROI. The schematic given in figure 2-1 illustrates the connection between crystal lattice deformation and a shift in the EBSD pattern as measured on the phosphor screen. The following geometrical relation is similar to that proposed by Wilkinson et al., but has been modified to more precisely represent the actual deformation geometry.

$$\frac{\vec{q}}{\lambda} = \vec{w} - (\vec{w} \cdot \hat{r}')\hat{r}' + \frac{\vec{q} \cdot \hat{r}'}{\lambda}\hat{r}' \qquad (2)$$

Here $\vec{q}$ is the shift in the EBSD patterns as measured on the phosphor, $\hat{r}$ is the unit vector pointing from the specimen origin to the ROI center on the phosphor screen, and $\hat{r}'$ points to the shifted position of the ROI in the deformed lattice pattern. λ is a geometrical factor and is given by $\lambda = \frac{z^*}{\hat{r}^{pc} \cdot \hat{r}}$ where $\hat{r}^{pc}$ is a unit vector normal to the

phosphor screen and z^* is the perpendicular distance from the screen to the sample origin. The displacement under deformation is represented by the vector $\vec{w}$, where $\vec{w} = A\hat{r}$. A is the displacement gradient tensor defined by $(A+I)=F$. F is the local deformation gradient tensor (its dependence upon location in the sample frame is implicit).

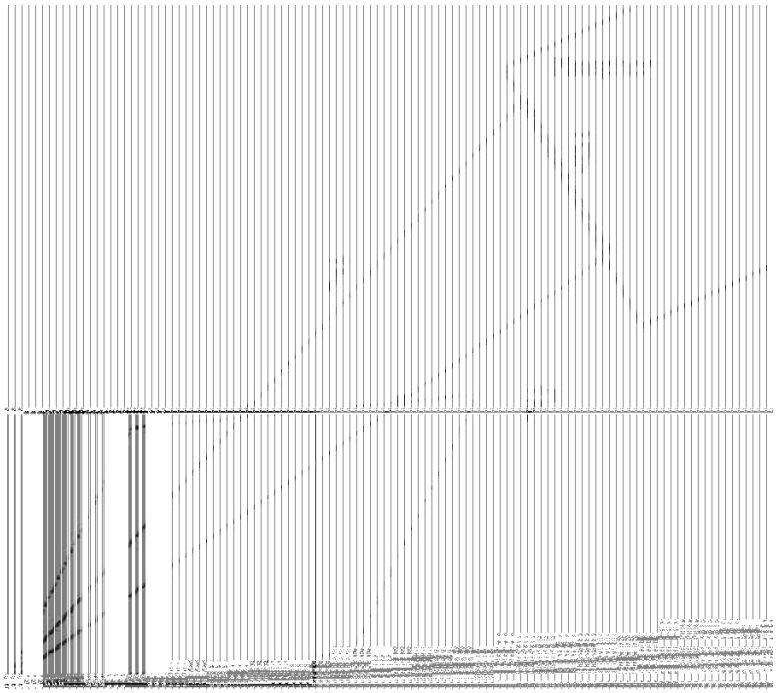

Figure 2-1: Schematic of how a strain and a rotation in the crystal lattice (greatly exaggerated) can be related to a shift of an EBSD pattern on the phosphor screen. The strained lattice is represented by the dashed line.

Equation (2) contains three independent equations, one for each component of $\vec{q}$ (the third component of $\vec{q}$ is uniformly zero when described in the coordinate frame of the phosphor screen, but is non-zero in other coordinate frames). Knowing the configuration of the microscope geometry and the appropriate coordinate frame transformations, $\hat{r}$ is easily calculated for any ROI. Using the measured shifts $\vec{q}$, $\hat{r}'$ can

also be evaluated. This leaves the displacement gradient tensor as the only unknown. Equation (2) is true for each ROI, and so can be used to formulate a system of equation. This system of equations can be used to solve for the off-diagonal components of the displacement gradient tensor, but not necessarily the diagonal components.

The diagonal components of the displacement gradient tensor correspond to normal elastic strains. Normal strains, or stretches and compressions of the lattice, do not necessarily cause a shift in the Kikuchi bands, so they are immeasurable by the cross-correlation method. A hydrostatic compression of the lattice causes the atomic planes to uniformly come closer together. In reciprocal space (which is what we see the EBSD patterns in), this compression of atomic planes corresponds to a widening of the Kikuchi bands. In terms of Bragg's Law, all that is changed is the d_{hkl} value; theta remains the same. The opposite is the case for a hydrostatic stretch of the lattice. Only the difference between diagonal components of the elastic strain tensor, or $[\varepsilon_{11} - \varepsilon_{33}]$ and $[\varepsilon_{22} - \varepsilon_{33}]$, causes shifts in the Kikuchi bands, and so is measurable by the cross-correlation. This issue is readily apparent in the Wilkinson derivation of the cross-correlation equations.

If boundary conditions are taken into consideration, it is possible to separate the diagonal components of the elastic strain tensor. EBSD patterns are collected from an interaction volume which is very near the surface of the sample (the electrons backscatter from a maximum depth of ~100 nm). At this depth, the normal direction to the sample surface can be assumed to be stress free. The stress can be related to elastic strain through Hooke's law. Mathematically, this can be expressed in the sample frame as:

$$\sigma_{i3}^{sample} = C_{i3kl}^{sample} \varepsilon_{kl}^{sample} = 0 \tag{3}$$

Or in the local crystal frame as:

$$\sigma_{ij}^{crystal} n_j = C_{ijkl}^{crystal} \varepsilon_{kl}^{crystal} n_j = 0 \tag{4}$$

Where n_j are the components of the vector normal to the sample surface given in the crystal frame.

If the elastic constants are known, Equation (4) provides the necessary additional equations to solve for the diagonal components of the elastic strain tensor.

For small deformations, the symmetric and asymmetric parts of the displacement gradient tensor A represent respectively the elastic strain and rotation according to the following equations:

$$\varepsilon = \frac{1}{2}(A + A^T) \text{ and } \omega = \frac{1}{2}(A - A^T) \tag{5}$$

The reader is reminded that the polar decomposition theorem enables the deformation gradient tensor, F, to be expressed as the product of a proper orthogonal tensor or rotation, R, and a positive definite symmetric tensor, U: $F=RU$. In the case of the small elastic deformations and rotations of the crystal lattice, ω can be related to the rotation tensor by $R = I + \omega$, and ε is related by the expression $U = I + \varepsilon$.

Care must be taken to express all terms in the above equations in the same reference frame - usually the deformed (or sample) frame or the reference (or crystal) frame. However, difficulties with the boundary condition are that, first the elastic

constants must be known, second the appropriate deformation must be known to express the elastic stiffness tensor, *C,* in the deformed frame. Conversely the appropriate deformation must be known to express $\hat{r}^{pc}$ in the crystal frame, but until the boundary condition equations are evaluated, the deformation is not completely known. This circular dependence may be resolved by an iterative process where an initial assumption is made about deformation, and then the calculated deformations are used to update subsequent iterations. This approach is described in detail later. The system composed of Equations (2) and (3) may be solved by choosing only two ROIs. (Note that this is a decrease in the number of requisite ROIs from Wilkinson's method because the system of equations includes the boundary conditions rather than imposing them after evaluation of the deformation geometry equation. However, this reduction is of limited technical significance because typically 10-20 ROIs are chosen to reduce the effects of noise and improve resolution.)

A new error measure was defined to describe the fit of a calculated deformation tensor to the shifts measured on the phosphor screen. To evaluate the fit, the shifts that would have been caused by a measured deformation tensor, *F*, are calculated, and then the average length of the difference between the calculated and measured shifts is found. For *N* ROIs in an EBSD pattern the error measure is defined as follows where ${}^{i}\hat{r}$ is the direction of the center of the i^{th} ROI, ${}^{i}\vec{q}^{m}$ and ${}^{i}\vec{q}^{c}$, are the measured and calculated shifts of the i^{th} ROI, *P* is the plane that contains the phosphor screen and $\bar{e}$ is the average error for all *N* ROIs.

$${}^{i}\vec{q}^{c} = {}^{i}\hat{r} - \left(F\,{}^{i}\hat{r}\right) \bigcap P \tag{6}$$

$$\bar{e} = \frac{1}{N}\sum_{i=1}^{N}\left|{}^{i}\vec{q}^{c} - {}^{i}\vec{q}^{m}\right| \tag{7}$$

The |…| notation in Equation (7) denotes the scalar magnitude, and $\bigcap$ in Equation (6) denotes the intersection of sets. The error measure $\bar{e}$ describes how well the calculated *F* fits the measured shifts.

2.2 Bragg's Law pattern simulations

Dependence on a reference pattern allows for measurements of elastic strain and orientation gradients, but makes it difficult to measure absolute values of elastic strain and orientation. This limitation can be solved by using simulated EBSD patterns that are generated at known lattice states. While high fidelity simulations are expected to compare best with collected images, computational costs make it favorable to utilize a simpler model. The development of simple Bragg's Law simulations is presented as well as evidence of their utility as reference patterns.

There are simple geometric relations that connect a crystal lattice state to its projected EBSD image, but in order to represent them mathematically several reference frames must be established. The first is the crystal frame, $\hat{e}_i^c$, with the local crystal lattice parameters defining the basis vectors (this reference frame is typically taken to be strain free—only the rotation component of the deformation tensor is used to rotate the global reference lattice vectors to the local lattice). The second is the standard sample frame ($\hat{e}_3^s$ normal to the sample surface, $\hat{e}_1^s$ in the rolling direction, and $\hat{e}_2^s$ in the transverse

direction). The sample frame is taken to be the external reference frame so that the rotation component of the local deformation tensor is exactly the orientation measured by traditional OIM. The third reference frame of interest is attached to the phosphor screen used to collect the EBSD images and is related to the pixilated image so that $\hat{e}_1^v$ points from left to right in the image (increasing columns), $\hat{e}_2^v$ points from top to bottom in the image (increasing rows) and $\hat{e}_3^v$ completes the orthonormal right-handed frame. A vector described in any of these three frames may also be rotated into another using a second rank tensor that describes a pure rotation. For example,

$$v_i^s = R_{ij}^{v \to s} v_j^v \tag{8}$$

Now consider the Bragg's Law relationship.

$$m\lambda = 2d_{hkl} \sin(\theta) \tag{9}$$

This law describes two cones of angle θ that bound the diffraction band from the *hkl* plane for a wavelength λ. *m* is an integer that denotes the order of the diffraction band. Only first order (*m*=1) diffraction bands are usually used, but higher order diffraction bands can be included with no fundamental modifications of the simulation method. The deformation tensor *F* determines how the diffraction cones are oriented with respect to the phosphor frame and may also change the inter-planar spacing d_{hkl}. Because the equation of a cone is easiest to describe in the frame in which it is a right rectangular

cone with the axis of symmetry in the *z*-axis, a fourth right-handed, orthonormal reference frame may be defined for convenience.

The cone reference frame is then aligned such that $\hat{e}_3^{co} = \hat{n}$, $0 = \hat{e}_2^{co} \cdot \hat{e}_3^{co}$, and $\hat{e}_1^{co} = \hat{e}_2^{co} \times \hat{e}_3^{co}$. In the cone reference frame, a point $\vec{p} = p_1\hat{e}_1^{co} + p_2\hat{e}_2^{co} + p_3\hat{e}_3^{co}$ lies on the cone if $p_1^{\,2} + p_2^{\,2} = \left(\frac{p_3}{\tan(\theta)}\right)^2$ where the angle is the same as in Equation (9). The CCD camera is made up of a matrix of pixels and each pixel can be described as a point in the cone reference frame. If a pixel falls on or between the two cones corresponding to a chosen refracting plane (*hkl*), then that pixel in the image of the simulated band, *B*, is taken to have an intensity equal to the square of the structure intensity, S_{hkl}, and zero otherwise.

$$B\left(\vec{p}, F, R^{v\to c}, R^{c\to co}, (hkl)\right) = \ldots$$
$$\begin{cases} S_{hkl}^2 & \text{if } \left(\left[R^{c\to co} F R^{v\to c}\vec{p}\right]_1\right)^2 + \left(\left[R^{c\to co} F R^{v\to c}\vec{p}\right]_2\right)^2 \geq \left(\dfrac{\left(\left[R^{c\to co} F R^{v\to c}\vec{p}\right]_3\right)}{\tan(\theta)}\right)^2 \\ 0 & \text{otherwise} \end{cases} \tag{10}$$

Summing the contributions of each band and its symmetry variants generates the complete approximation of the EBSD pattern image. If S^i are the elements of the symmetry subgroup and $(hkl)^{(j)}$ are the elements of the set that includes all of the diffracting planes, then the composite simulation image can be described as follows.

$$I(\vec{p},F) = \sum_i \sum_j B(\vec{p},F,S^{(i)}(hkl)^{(j)}) \tag{12}$$

Figure 2-2 shows a collected pattern from a single crystal silicon sample and a simulated pattern generated at the OIM calculated orientation. The simulated pattern has the following input parameters:

a) Diamond structure lattice, a = 5.43Å

b) 70° Sample tilt angle

c) 10° elevation angle of phosphor screen

d) Phosphor screen width D_x = 1000 pixels and height D_y = 1000 pixels

e) Pattern center (from lower left corner) $PC_x = 0.5405\ D_x$, $PC_y = 0.7139\ D_x$

f) Sample to phosphor screen distance $z^* = 0.7455\ D_x$

g) Orientation in Euler angles (radians): $\varphi_1 = 1.74$, $\Phi = 3.06$, $\varphi_2 = 0.11$

Furthermore, both patterns were filtered using a band pass filter.

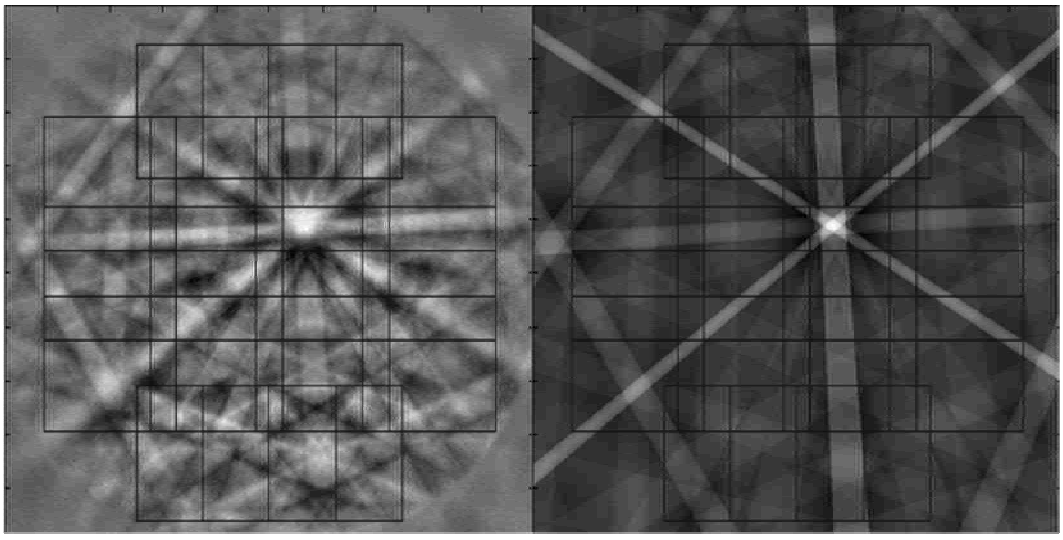

Figure 2-2: Collected pattern (left) and a simulated pattern (right) at approximately the same orienation with outlines of ROIs drawn on.

2.3 Simulation of deformed lattice

When simulating EBSD patterns from a deformed lattice, care must be taken to calculate both the plane normal of the deformed plane and the new d_{hkl} correctly. We define three orthogonal vectors $\vec{a}$, $\vec{b}$, and $\vec{c}$. $\vec{a}$ and $\vec{b}$ lie in the basal plane of the lattice. $\vec{c}$ is normal to that plane. In the case of a cubic lattice, $\vec{a}$, $\vec{b}$, and $\vec{c}$ correspond to the lattice vectors. We can also define the plane normal $\hat{n}$ by $\hat{n} = \frac{\vec{a} \times \vec{b}}{|\vec{a} \times \vec{b}|}$. The deformation of the lattice is described by the deformation gradient tensor *F*. The deformed vectors $\vec{a}$, $\vec{b}$, and $\vec{c}$ can be described post deformation by $\vec{a}' = F\vec{a}$, $\vec{b}' = F\vec{b}$, and $\vec{c}' = F\vec{c}$. Note that the vectors $\vec{a}'$, $\vec{b}'$, and $\vec{c}'$ are not necessarily orthogonal to each other.

The derivation of the following equation describing a plane normal after deformation can be found in standard mechanics books [22]:

$$|\vec{a}' \times \vec{b}'|\,\hat{n}' = |\vec{a} \times \vec{b}|\,\det(F)(F^{-1})^{T}\,\hat{n} \tag{13}$$

Here $\hat{n}'$ is the unit vector associated with the normal to the deformed plane and replaces $\hat{n}$ when calculating $\hat{e}_3^{co}$ above. The new d_{hkl} is found using the dot product and is given by $d_{hkl} = \vec{c} \cdot \hat{n}'$.

2.4 Strain and rotation analysis with simulated patterns

It was found during the development process of the simulated pattern method that a single comparison between a measured and simulated EBSD pattern using the cross-

correlation technique did not give the desired angular and strain resolution. To improve the resolution, an iterative technique was developed using the Hough measured orientation as the starting point. The iterative technique also allows for updating the boundary conditions by more accurately identifying with each iteration the normal to the sample surface. The simulated pattern analysis algorithm proceeds as follows:

1) Measure a local lattice orientation to within a 0.5° using the Hough transform method and save the EBSD pattern image
2) Generate a simulated pattern based on the crystal structure (which must be known) and the Hough-transform estimate of the true orientation
3) Use the cross-correlation analysis algorithm to compare shifts from the simulated pattern to the saved EBSD pattern image
4) Calculate the deformation tensor by inputting the measured shifts into Equations (2) and (3) and solving
5) Evaluate the fit of the deformation tensor with Equation (7)

At the conclusion of these five steps, a new pattern can be simulated at a deformation state that is closer to the actual state of the examined material. If the refined simulation pattern is then used for steps 3-4, the error measure significantly improves. By repeating this process iteratively, a solution for the deformation tensor is rapidly converged upon.

2.5 Pattern center calibration

In order to obtain accurate results from the simulated pattern method, the patterns must be simulated with an accurate pattern center. The pattern center is defined as the intersection of a vector originating from the electron beam/sample interaction point and normal to the plane of the phosphor screen (figure 2-3). For calibration purposes, the sample to phosphor screen distance is also included as the z coordinate of the pattern center. Standard EBSD analysis software packages include pattern center calibration routines. These calibration routines generally use a least squared approach to find the best fit for the pattern. The fit is defined as the angular deviation between the detected bands from a measured pattern and the calculated position of the bands based on the measured orientation. This calibration is carried out on four corners of a low magnification square to find the variation in pattern center as the electron beam rasters across the sample. While sufficiently accurate for the purposes of OIM, this calibration is not of sufficient precision for high resolution cross-correlation methods.

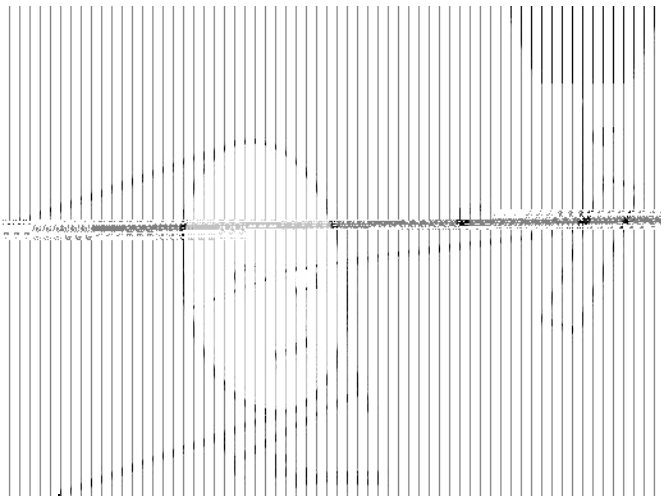

Figure 2-3: Pattern center schematic.

An optimization routine was set up in Matlab to calibrate a more refined pattern center for each scan. The main issue to address in optimizing the pattern center is finding a suitable variable to minimize in the optimization. It was found that minimizing the norm of the elastic strain tensor, where the norm is defined as the sum of the squared components, gave the best results. However, upon experimentation with simulated pattern comparisons it was also found that an error in pattern center calibration can exactly mimic the shifts caused by actual strains and rotations of the crystal lattice. Consequentially, if a collected EBSD pattern from a strained portion of the lattice is used as the calibration pattern, artificially low elastic strains can be measured and the pattern center will still be poorly calibrated.

In order to address this issue, a special sample holder was built for the SEM (figure 2-4). The sample holder allows for two samples to be mounted coplanar with each other. One of the samples is the sample of interest and the other is a reference single crystal sample that is assumed to be strain free. A strain free assumption is justifiable since it is expected that any elastic strains present will be below the resolution limit of the simulated pattern method and should not affect any measurements. A square scan is taken on the single crystal sample and the patterns are saved. The stage is then shifted over (just using the horizontal stage control so that the scan geometry does not change) and the sample of interest is scanned.

The square scan from the single crystal sample is used for calibration purposes. For each measured pattern from the single crystal sample, the pattern center is calibrated by minimizing the norm of the elastic strain tensor calculated when comparing the measured pattern to a simulated pattern of specified pattern center. The pattern center that

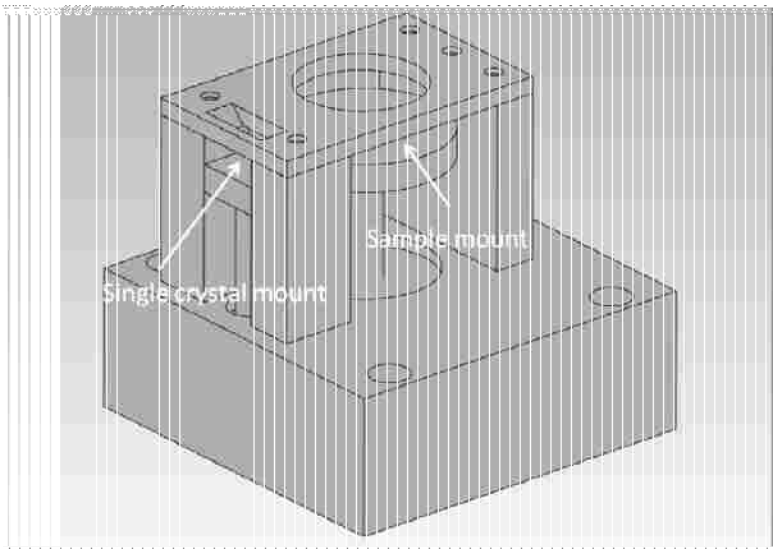

Figure 2-4: Model of custom SEM stage

minimizes the norm of the elastic strain tensor is found using a built in Matlab optimization routine that minimizes a chosen function using the Nelder-Mead simplex method [23]. The Nelder-Mead simplex method begins with an n-dimensional simplex where n is the number of variables. The simplex has n+1 vertices where each vertex corresponds to a set of variables. The function is evaluated at each vertex, and based on set criteria, one vertex is eliminated. A new simplex is formed keeping all but one vertex the same, and the process is repeated. Eventually, the simplex converges on the set of variables that minimizes the function. In the case of minimizing the elastic strain for pattern center calibration, the variables are the x and y coordinates of the pattern center and the sample to phosphor screen distance. The pattern center calibration is used to find both the absolute pattern center and the pattern center variation as the electron beam rasters across the sample surface.

2.6 Pattern filtering

Before analyzing an EBSD pattern using the simulated pattern method, the pattern is filtered and processed to improve convergence and accuracy. Any defects or non-uniformity of EBSD patterns can have a detrimental effect when using a cross-correlation-based technique. They can cause the cross-correlation function to measure shifts that match the defects instead of finding the shifts that align the Kikuchi bands.

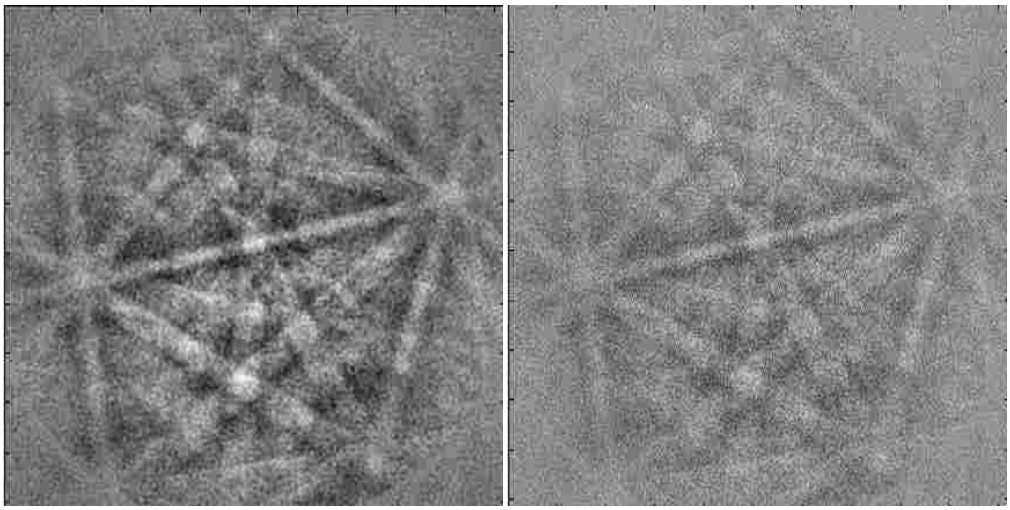

Figure 2-5: Comparison of filtered (left) and non-filtered (right) EBSD patterns.

Using simulated patterns for the reference pattern limits the defects to only one of the two patterns being compared using cross-correlations. This lessens the effect that small pattern defects can have on the results, but does not eliminate it. Special care must be taken to eliminate as much as possible any detrimental pattern defects without filtering out too much information.

Image processing is done using two different techniques: background subtract and band pass filtering. The image processing improves convergence by eliminating or

minimizing intensity gradients from the overall EBSD pattern, filtering out background noise, and improving the contrast of the Kikuchi bands (figure 2-5).

Background subtract is done using a built in OIM option. A number of patterns are collected from the sample at the same operating conditions as the scan. The pattern intensities are averaged to form a "background" pattern. This background is then subtracted from each pattern in the scan. Two aims are achieved through this background subtraction. First, any defects on the phosphor screen are present in the background pattern, and so are subtracted out from all other patterns. Second, EBSD patterns naturally have a non-uniform intensity distribution. There is a peak intensity at the spot of highest electron interaction, and the intensity fades away from there. The background subtract flattens this intensity and makes it more uniform across the pattern.

3 Sensitivity Analysis

A series of tests was performed to evaluate the resolution limits of the simulated pattern method and its sensitivity to any calibration errors. Before describing the tests and results, it is appropriate to define exactly what is meant by resolution in the case of the simulated pattern method.

3.1 Resolution considerations

There are three main types of resolution that could be considered when discussing EBSD-based techniques: spatial, angular, and strain. The spatial resolution of an EBSD scan is based on the step size used when taking the scan. The limiting spatial resolution is determined by the interaction volume of the electron beam in the sample. The interaction volume is dependent on a number of factors including, but not limited to, the accelerating voltage of the electron beam, the acquisition time for each EBSD pattern, and the atomic mass of the material. A spatial resolution of 20-50 nm is generally reported for EBSD techniques. No attempt is made in this paper to discuss ways to increase the spatial resolution of EBSD-based techniques.

The meaning of angular and strain resolution, as used in this paper, is the uncertainty in the data. In other words, the collected data are accurate to within plus or minus the reported resolution limit. The angular and strain resolution can be further

broken down into two categories describing a global resolution limit and a resolution of the gradient between points. The global resolution describes how much the data as a whole may be offset in either strain or rotation. This resolution is limited mainly by the accuracy of geometry calibrations. The resolution of the gradient describes how accurately the change in orientation or strain is measured between adjacent points.

3.2 Resolution limits

A series of tests was performed to evaluate the angular and strain resolution of the simulated pattern method.

3.2.1 Convergence of iterations

The first test carried out was simply to observe the variations of elastic strain and orientation between iterations once convergence was reached. For this purpose, a pattern

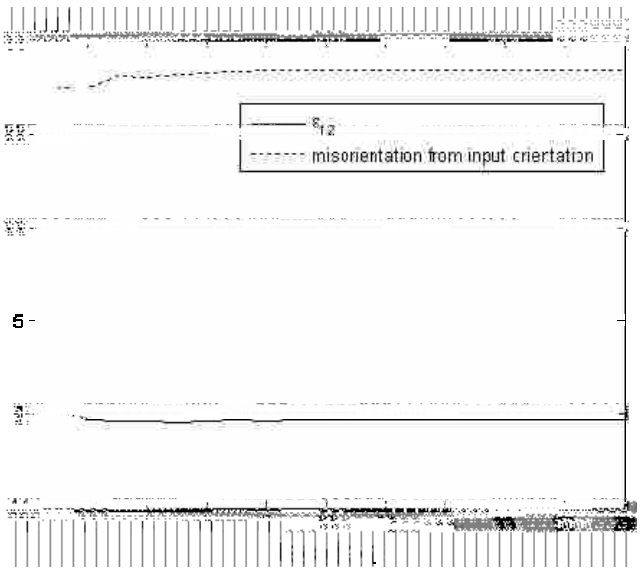

Figure 3-1: Convergence of orientation and strain. y-axis is in radians for orientation and unitless for the strain component.

from a single crystal germanium sample was collected at a camera resolution of 512x512 pixels and analyzed using the simulated pattern method. The analysis was allowed to run for 20 iterations (figure 3-1).

The suggested angular resolution is taken to be the variation in elastic strain and orientation averaged over the last 10 iterations. The results suggest an angular resolution of (6.1×10^{-4}) ° and a strain resolution of 6.1×10^{-6}.

3.2.2 Simulated/simulated pattern comparisons

The second test performed was a comparison of simulated patterns generated at slightly different lattice states. A strain free EBSD pattern was generated, and then another strained pattern was generated at a rotated orientation. The test was carried out using 512x512 pixel simulated α-iron patterns. Table 3-1 shows a list of input and measured deformation tensors. The tensors were then decomposed to estimate the resolution of the elastic strain and orientation separately. Since the test was performed in an entirely computational environment, the traction free boundary condition does not apply, and so the diagonal components of the elastic strain tensor were ignored.

The results suggest a strain resolution of 1×10^{-3} and an angular resolution of 0.05° for large deformations (components of $F>0.02$). For smaller deformations, the results suggest a strain resolution of 1×10^{-4} and an angular resolution of 0.0045°. This test is not meant to be statistically significant, but instead to give a general idea of what limiting resolution we might expect from the iterative cross-correlation approach.

Table 3-1: Simulated pattern comparisons for resolution estimation

Input F	Calculated F	Maximum error in elastic strain	Error in rotation
$\begin{bmatrix} 0 & 0.01 & -0.01 \\ 0.02 & 0 & 0.02 \\ 0.01 & 0.02 & 0 \end{bmatrix}$	$\begin{bmatrix} 0 & 0.0096 & -0.0096 \\ 0.0186 & 0 & 0.0194 \\ 0.01 & 0.02 & 0 \end{bmatrix}$	$1x10^{-3}$	0.049°
$\begin{bmatrix} 0 & 0.001 & -0.003 \\ 0.002 & 0 & 0.0001 \\ -0.001 & 0.0006 & 0 \end{bmatrix}$	$\begin{bmatrix} 0 & 0.001 & -0.003 \\ 0.0021 & 0 & 0.0001 \\ -0.001 & 0.0006 & 0 \end{bmatrix}$	$1x10^{-4}$	0.003°
$\begin{bmatrix} 0 & 0 & -0.01 \\ 0.02 & 0 & 0.0001 \\ 0.001 & 0.0006 & 0 \end{bmatrix}$	$\begin{bmatrix} 0 & 0.0001 & -0.0101 \\ 0.02 & 0 & 0.0000 \\ 0.001 & 0.0006 & 0 \end{bmatrix}$	$1x10^{-4}$	0.0045°

3.3.3 Beam shift experiment

The beam shift experiment was used to test the ability of the cross-correlation function to measure shifts when comparing simulated patterns to measured patterns. An EBSD pattern was generated at approximately the same lattice state as a collected pattern from a single crystal silicon sample. The silicon pattern was collected at the full camera resolution of 1000x1000 pixels. The simulated pattern was shifted a known number of pixels and compared to the measured pattern using the cross-correlation function to measure the applied shift. This was repeated several times for increasing shifts of the simulated pattern. Figure 3-2 shows the shifts applied to the simulated pattern and the corresponding measured shifts in both the horizontal and vertical directions. The cross-correlations correctly identified the shifts to within 0.05 pixels, and the standard deviation

of the measured shifts from the applied shifts was 0.035 pixels. It can be seen that the spread in the measured shifts was smaller in the horizontal direction than in the vertical direction, but the exact reason for this is unknown. Deviations of a collected pattern from a simulated pattern should then be measurable to $1/20^{th}$ of a pixel, which is the same level of resolution claimed by Wilkinson for the cross-correlation method [12].

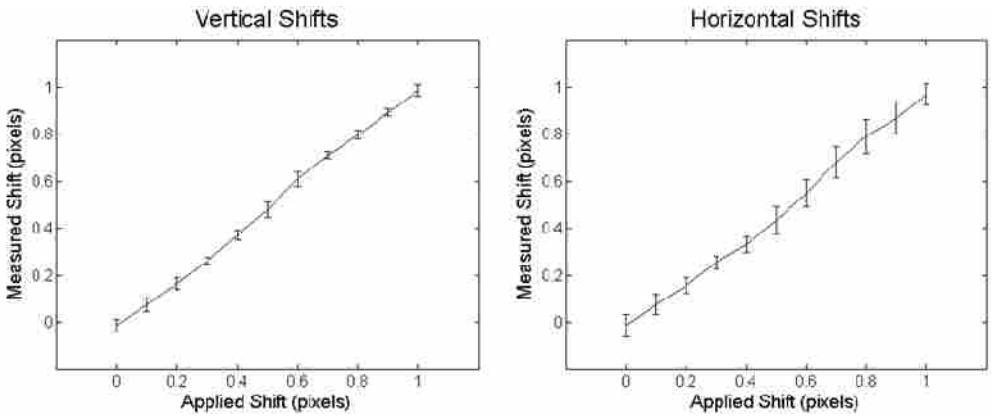

Figure 3-2: Measured shifts when comparing simulated and measured EBSD patterns

An EBSD pattern covers about 1.05 radians of angular space of the full Kikuchi map. Using this, the shift resolution can be correlated to an angular and strain resolution. An error of $1/20^{th}$ of a pixel corresponds to a strain resolution of 5.3×10^{-5} and an angular resolution of 0.003°.

3.3.4 Rotation test

In the next test, a rotation was applied incrementally to a sample in the microscope chamber and five patterns were collected at each increment of rotation. The rotation control of the stage does not have sufficient precision to adequately probe the

resolution of this method, so instead the standard deviation of the five measurements at a constant angle of rotation was taken to be the resolution limit. This test was performed using a single crystal [0 0 1] silicon sample (figure 3-3).

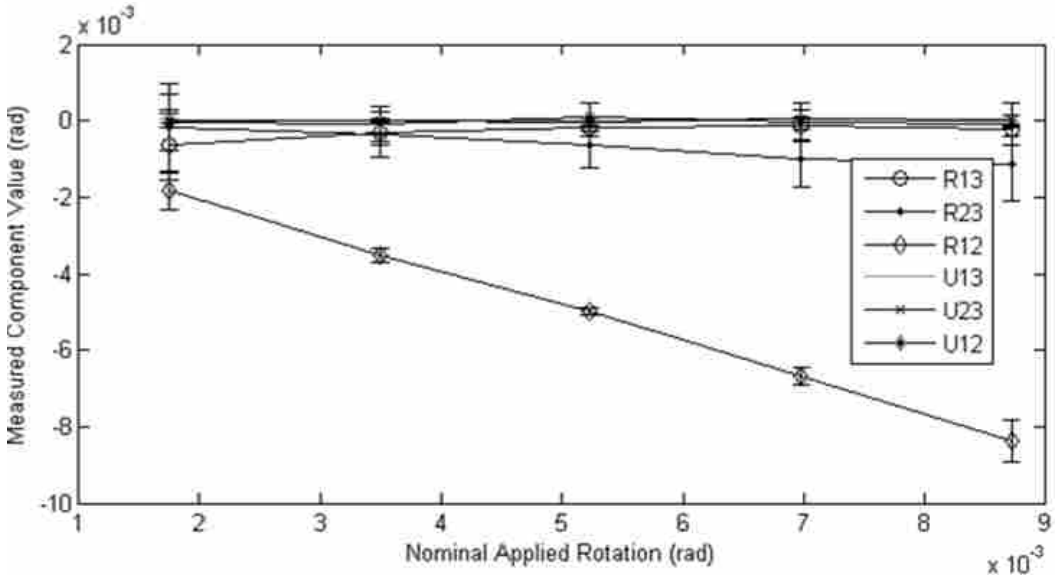

Figure 3-3: Rotation test of resolution of the simulated pattern method

The results suggest an angular resolution of 0.02° and a strain resolution of 3.6×10^{-4}.

The worst resolution suggested by the resolution tests is 0.02° angular resolution and a strain resolution of 3.6×10^{-4} for small strains and 1×10^{-3} for large (>0.02) strains.

3.4 Resolution sensitivity to geometry calibration

Errors in the geometry inputs for pattern simulations can lead to both global and local errors when using the simulated patterns as reference patterns for deformation

calculations. A correct knowledge of the SEM geometry is vital for accurate EBSD pattern simulations. Incorrect geometry parameter inputs in the pattern simulations can cause the simulated pattern to be shifted, dilated, or expanded relative to the measured pattern. As a result, shifts are measured in the ROIs that do not correspond to an actual strain or rotation of the crystal lattice, and an incorrect displacement gradient tensor is calculated.

The following geometry parameters must be correct in the simulation in order to obtain accurate measurements of strain and rotation: elevation angle, sample tilt angle, x and y position of the pattern center, and the sample to phosphor screen distance.

Both the elevation angle and sample tilt angle influence only the global orientation measurements of the lattice. Typical SEM systems allow for the elevation and sample tilt angles to be known to ~0.1°, causing a comparable error in the measured orientation of the crystal. Since both angles are constant (assuming a planar sample surface), they do not affect the misorientation measured between points in a scan. For the majority of applications of microstructure analysis, a resolution of 0.1° for the absolute orientation is sufficient as long as the misorientation is not affected. No attempt is made to calibrate the sample tilt or elevation angle.

The pattern center is defined as the intersection of a vector originating from the electron beam/sample interaction point and normal to the plane of the phosphor screen. For calibration purposes, the sample to phosphor screen distance is also included as the z coordinate of the pattern center. The pattern center varies depending on the interaction point of the electron beam with the sample, and so must be found for every point in the scan. The pattern center is a purely geometrical parameter, and so, assuming that the

sample is planar, these variations should be linear with the change in position of the electron beam.

The sensitivity to error in the pattern center calibration on the measured values of elastic strain and rotation was investigated by comparing simulated patterns to each other. In this study, a strain free pattern was simulated and used as a reference pattern. Subsequent patterns were then simulated keeping everything identical to the reference pattern except for the pattern center. The patterns were then compared using the simulated pattern method to find how errors in the pattern center correspond to errors in the components of the elastic strain and rotation tensors (figure 3-4 and 3-5).

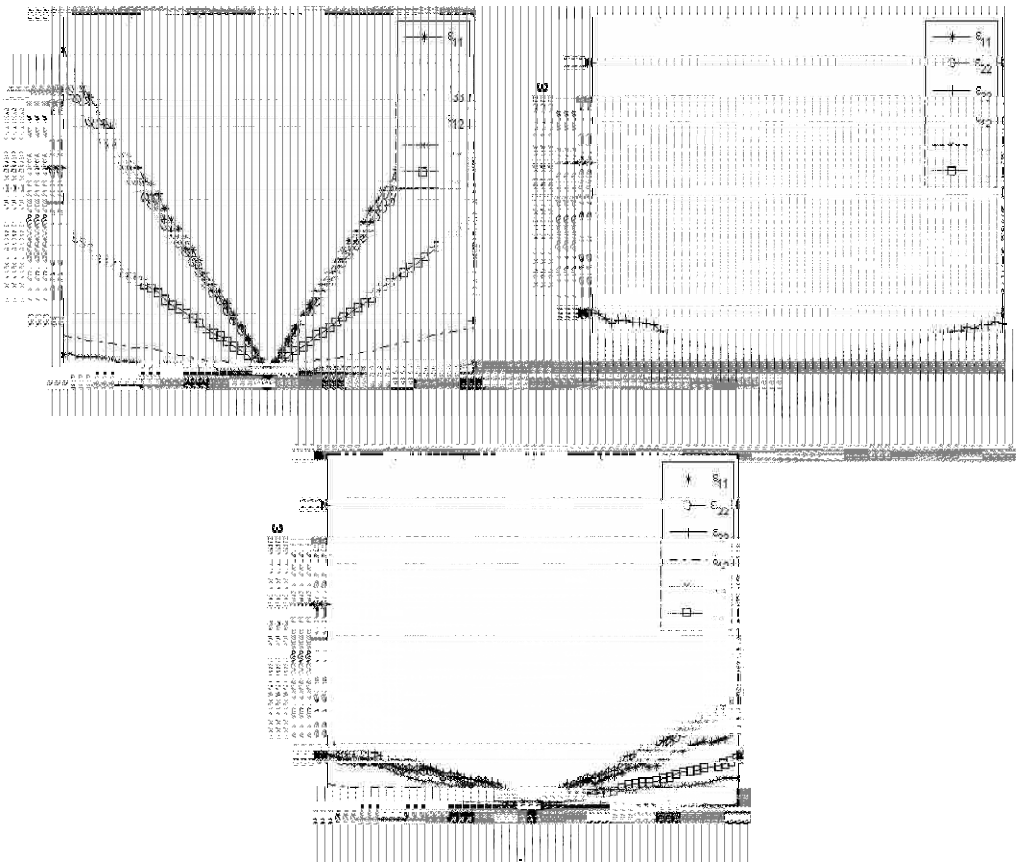

Figure 3-4: Relation of error in elastic strain components to error in pattern center calibration

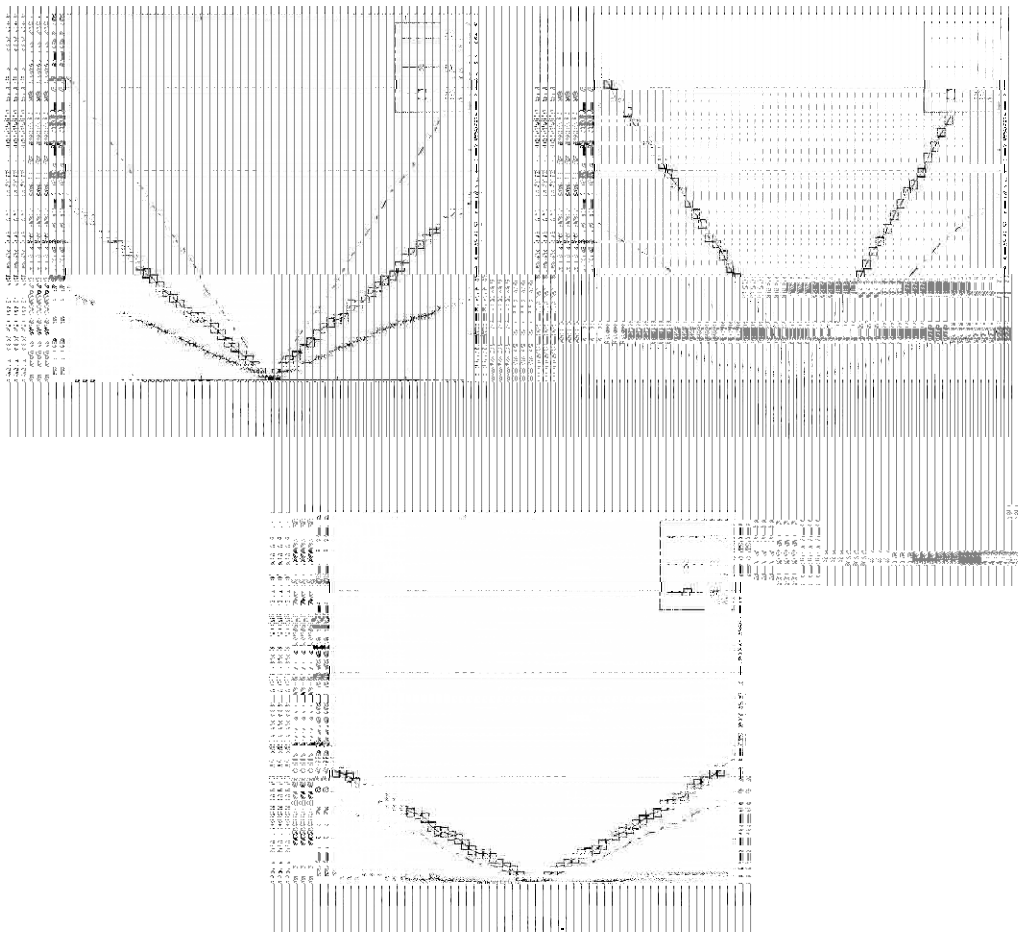

Figure 3-5: Relation of error in rotation tensor components to error in pattern center calibration

As can be seen from the results, the elastic strain calculations are most sensitive to the sample to phosphor screen distance, and the lattice orientation calculations are most sensitive to error in the x and y coordinates of the pattern center. The diagonal components of the elastic strain tensor, which correspond to a normal strain, are the most sensitive to errors in the phosphor to screen distance. Measurements of the tetragonality of a material are taken from the diagonal components of the elastic strain tensor, so it is especially important that this distance be calibrated accurately.

A method for pattern center calibration was described in chapter 2. A series of tests was performed to evaluate the accuracy of the pattern center calibration for strain and orientation resolution determination.

3.4.1 Accuracy of OIM pattern center calibration

To begin with, a simple test was carried out to get a rough estimate of the accuracy of the OIM calibrated pattern center. The pattern center was calibrated using a series of patterns collected from a single crystal germanium sample. The patterns were collected in a horizontal line across the sample, so only variations in PC_x should occur.

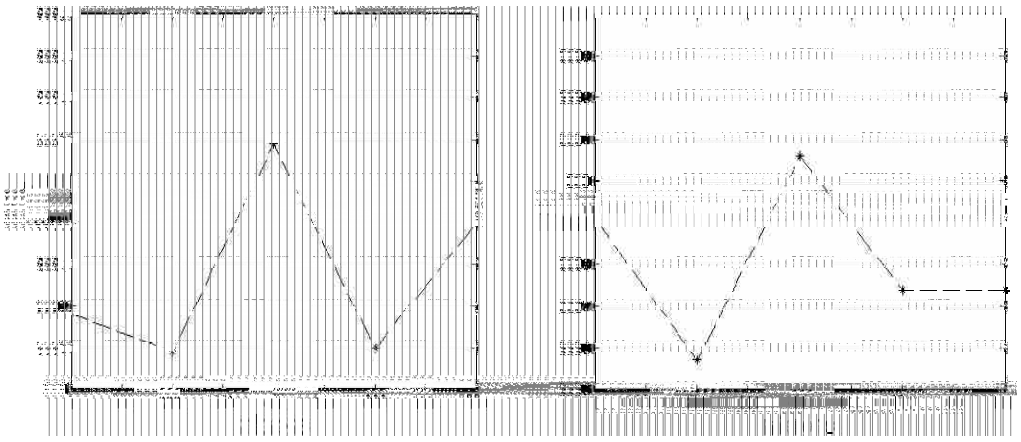

Figure 3-6: Variations in pattern center as measured by OIM as beam moves in x direction on sample

The pattern center was calibrated for eight patterns collected from a strain free germanium single crystal. As can be seen from figure 3-6, the scatter in the data for both z* and PC_y is ~0.005$D_{phosphor}$. Using figure 3-4 and 3-5**,** this error can be related to an error in the elastic strain of ~0.005. This error is well above the resolution limit of the

simulated pattern method, emphasizing the importance of a more precise pattern center calibration.

3.4.2 Comparison to theoretical variations

Assuming a perfect knowledge of the geometry of the SEM, the variations in the pattern center can be predicted. Admittedly, such a perfect knowledge is unobtainable with current SEM configurations, but a theoretical prediction of pattern center shifts can still be profitably compared to measured variations to ensure that the measured variations are at least somewhat accurate.

For the derivation of the variation in pattern center with beam movement, the following terms are defined:

ΔPC_x = variation in *x* coordinate of pattern center

ΔPC_y = variation in *y* coordinate of pattern center

Δz^* = variation in sample to phosphor screen distance

Δx = movement in *x* on sample surface

Δy = movement in *y* on sample surface

$D_{phosphor}$ = diameter of the phosphor screen

$\theta = 90°$ - sample tilt angle

φ = elevation angle

The sample is assumed to be perfectly planar and tilted only about one axis (θ). With these assumptions, ΔPC_x varies only with changes in *x* in the beam position, and

ΔPC_y and Δz^* vary only with changes in *y* in the beam position. We wish to find the changes in pattern center with changes in beam position, or $\frac{\Delta PC_x}{\Delta x}$, $\frac{\Delta PC_y}{\Delta y}$, and $\frac{\Delta z^*}{\Delta y}$.

The change in PC_x is equal to the change in the *x* position on the sample, so we can write the relation $\frac{\Delta PC_x}{\Delta x} = \frac{1}{D_{phosphor}}$. The $\frac{1}{D_{phosphor}}$ term is a unit conversion used to express Δx as a fraction of the phosphor screen (this is the generally used form for expressing the pattern center).

$\frac{\Delta PC_y}{\Delta y}$ is found by defining a new term Δy_z. This term is defined by the geometry shown in figure3-7.

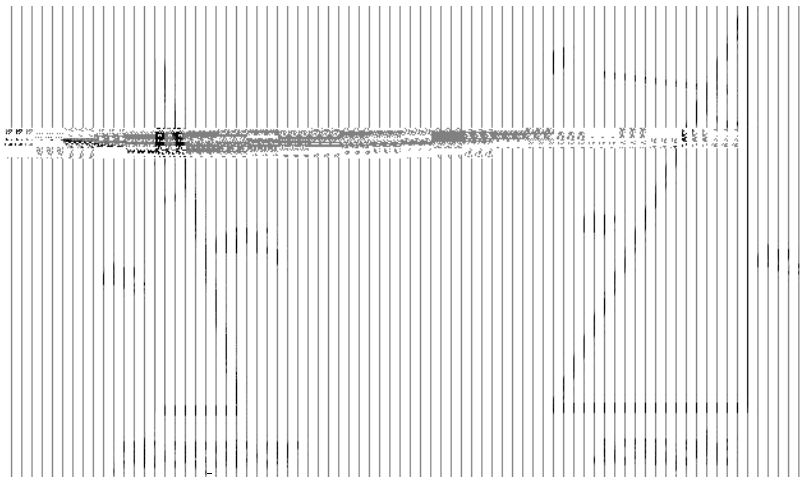

Figure 3-7: Geometry of y-component of pattern center

Δy_z can be solved for from both the phosphor screen and sample geometry using basic trigonometry. From the phosphor, we have:

$$\Delta PC_y = \Delta y_z \cos\varphi \tag{14}$$

and from the sample we have:

$$\Delta y_z = \frac{\Delta y \cos\theta}{D_{phosphor}} \tag{15}$$

Solving both for Δy_z and setting them equal to each other, we get:

$$\frac{\Delta PC_y}{\cos\varphi} = \frac{\Delta y \cos\theta}{D_{phosphor}} \tag{16}$$

We can then solve for $\frac{\Delta PC_y}{\Delta y}$ giving us:

$$\frac{\Delta PC_y}{\Delta y} = \frac{\cos\theta}{D_{phosphor}\cos\varphi} \tag{17}$$

Similarly, the geometry to find $\frac{\Delta z^*}{\Delta y}$ is given in figure 3-8

From the geometry, $\frac{\Delta z^*}{\Delta y}$ is found using trigonometry:

$$\frac{\Delta z^*}{\Delta y} = \frac{\sin(\theta+\varphi)}{D_{phosphor}} \tag{18}$$

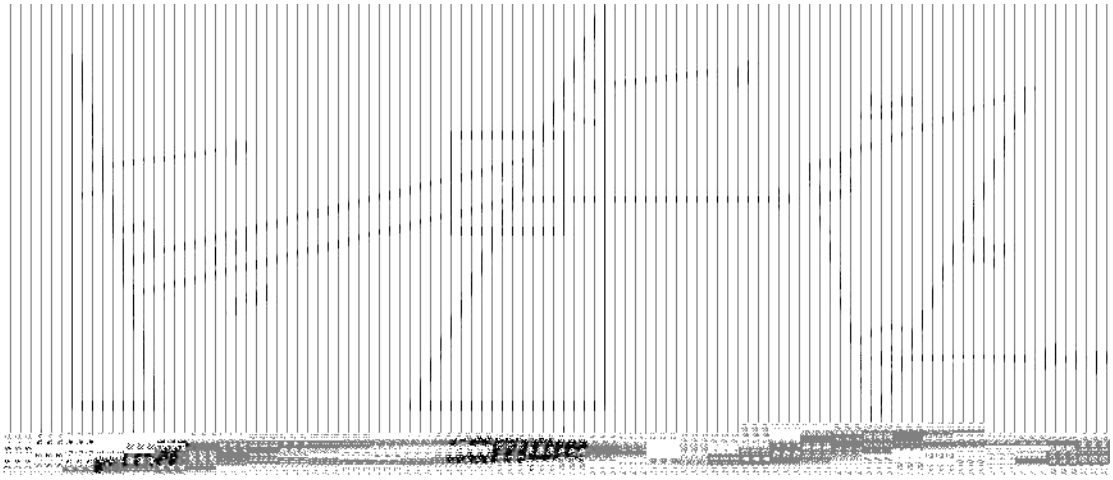

Figure 3-8: Geometry of z-component of pattern center

A 1x1 mm square scan with a 0.1 mm step size was collected from a single crystal germanium sample. At each point, the pattern center was calibrated using the method described in chapter 2. The change in pattern center with change in beam position was found and compared to the theoretical variations using a measured phosphor screen diameter of 37 mm. Both the theoretical and measured lines are plotted together for comparison in figure 3-9**.**

We can compare the slope of the theoretical line with a best fit line generated for the calibrated pattern center. The y-axis is in the standard units that EBSD systems use (% $D_{phosphor}$). The x-axis is in units of microns. The patterns used for the pattern center calibration were binned to 512x512 pixels. So, to convert the slope to pixels/μm, we can multiply it by 512.

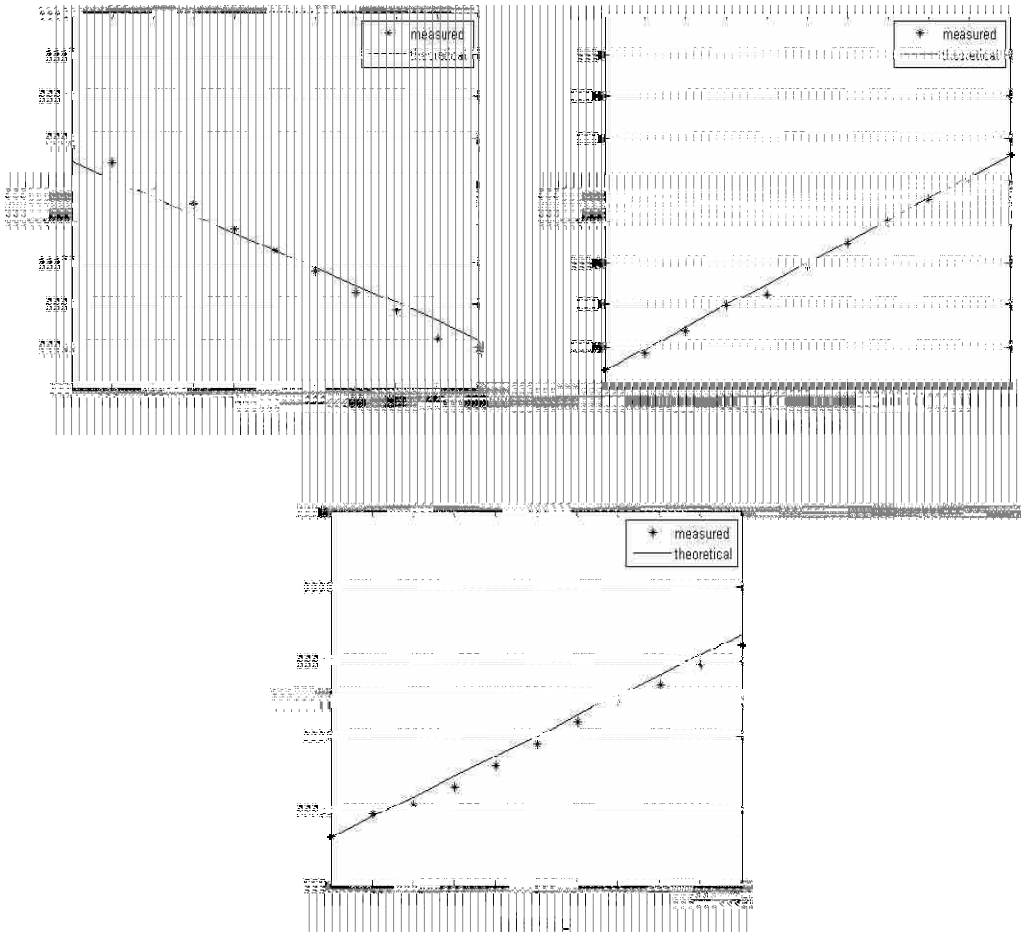

Figure 3-9: Measured variation of pattern center compared to theoretical

PC_x Theoretical slope = -2.7027×10^{-5}

Measured slope = -2.7158×10^{-5}

PC_y Theoretical slope = 2.5789×10^{-5}

Measured slope = 2.6086×10^{-5}

z* Theoretical slope = 1.3514×10^{-5}

Measured slope = 1.2919×10^{-5}

So, what does this mean? On average, the difference between the theoretical and measured slope is $3x10^{-7}$. If we assume that the geometry really is exactly what we assumed that it is when calculating the theoretical slopes, it means that for every 100 μm step, we are measuring the variation in pattern center to within ~0.015 pixels. The simulated pattern code can use this measured slope to calculate a varying pattern center as the input for the pattern simulations.

The calibration of the absolute pattern center at a given point is much more difficult to verify. Simulated/simulated pattern comparisons give a rough idea of the calibration resolution, but the results do not necessarily mean that the same resolution can be expected when comparing simulated and measured patterns for pattern center calibration.

3.4.3 Calibration with simulated patterns

A computational verification of the pattern center calibration technique was carried out using simulated pattern comparisons. Two different patterns were simulated with slightly different pattern centers and at slightly different orientations (0.5° difference in orientation). Both patterns were simulated with zero elastic strain. This situation was meant to simulate the conditions of calibrating the pattern center on a strain free single crystal sample using the Hough measured orientation as the input orientation for the pattern simulation. The test was carried out for a number of different input pattern center errors. Table 3-2 shows the results for the pattern center error after calibration.

Table 3-2: Resolution of pattern center calibration

Correct Pattern Center			Input Pattern Center			Output Pattern Center		
PC_x	PC_y	z*	PC_x	PC_y	z*	PC_x	PC_y	z*
0.5011	0.7293	0.7586	0.5011	0.7293	0.7486	0.5000	0.7296	0.7586
0.5011	0.7293	0.7586	0.5011	0.7393	0.7586	0.5001	0.7296	0.7586
0.5011	0.7293	0.7586	0.4911	0.7293	0.7586	0.5001	0.7296	0.7585
0.5011	0.7293	0.7586	0.5081	0.7233	0.7556	0.5000	0.7296	0.7585

From the table, the average error in each component of the pattern center is 0.0010 for PC_x, 0.0003 for PC_y, and $<5x10^{-5}$ for z*. Using the graphs in figure 3-4 and 3-5, this corresponds to a rotational error of 0.001 radians, or 0.057° and a negligible error in the elastic strain. The rotational error is a global error in the data, meaning that it does not affect the angular resolution of the method when measuring misorientations between points.

4 Dislocation Density Measurements in Mg AZ91

4.1 Dislocation density: resolution considerations

EBSD-based texture analysis techniques have been utilized with success by various researchers to obtain estimates of the local dislocation density in a material. The theoretical groundwork for dislocation density estimates is largely based on the work of Nye [24]. He was able to show how the lattice curvature, or curl of the orientation field, could be linked to geometrically necessary dislocations. Later work by Kröner [25] advanced Nye's work to include the elastic strain in the formulation. The following equation emerged:

$$\alpha_{ik} = \kappa_{ki} - \delta_{ki}\kappa_{pp} + e_{klj}\varepsilon^{e}_{ij,l} \tag{19}$$

where κ_{ki} is the lattice curvature tensor, ε^{e}_{ij} is the elastic strain tensor, and α_{ik} is the dislocation density tensor. The components of the dislocation density tensor weight the dyadic formed by the direction of the dislocation line and the Burger's vector characterizing that dislocation. An important distinction needs to be made between two different types of dislocations when discussing dislocation densities. There are geometrically necessary dislocations (GND) and statistically stored dislocations (SSD).

SSDs come in pairs with opposite signs (Burger's vectors pointing in opposite directions), and have no long range effect. Only GNDs contribute to curvature over a grain. When estimating dislocation densities using EBSD-based techniques, each square of data points forms a Burger's circuit (figure 4-1) [26, 27]. Kröner's formula is used to estimate the net dislocation effect within the circuit. The formula is not sensitive to any SSDs contained within the circuit. However, if a small enough Burger's circuit is used, i.e if a small enough step size is used when collecting data points, all SSDs effectively become GNDs and can be detected.

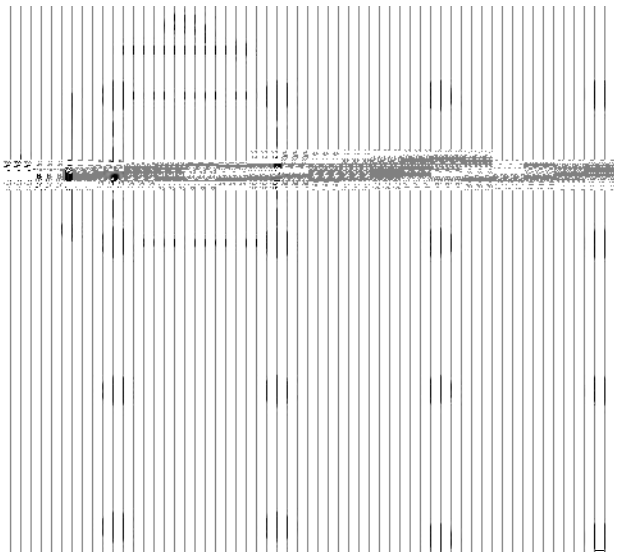

Figure 4-1: Representation of Burger's circuit formed using EBSD data points

Since the dislocation density estimates are dependent on spatial derivatives of the orientation field, they are very sensitive to the angular resolution of the chosen characterization technique. Noise in the data can be reduced by increasing the step size

between data points, but, as is usually the case, there is a tradeoff. As the step size increases, more SSDs are averaged out and so they are undetected [28].

All this should be taken into account along with the expected dislocation density when choosing a step size. If too small of a step size is used, the data will be dominated by noise. If too large a step size is used, important data will be averaged out.

The three techniques discussed in this paper are Wilkinson's cross-correlation method, the simulated pattern method, and traditional OIM. They have estimated angular resolutions of 0.006°, 0.02°, and 0.5° respectively. The theoretical minimum local dislocation density that can be measured without the data being dominated by noise is given by:

$$\rho_{\min}^{GND} = \frac{\theta_{\min}}{Lb} \tag{20}$$

where $\theta_{\min}$ is the limiting angular resolution of the chosen method in radians, L is the step size, and b is the magnitude of the Burger's vector.

Figure 4-2 provides a reference as to what should be taken into account when interpreting data from dislocation density estimates. Assuming a Burger's vector of 2.5 Å, the minimum resolvable dislocation density is plotted as a function of step size for each of the discussed methods. The interpretation of the plot is that any dislocation density that falls below the minimum resolvable dislocation density line will be dominated by noise, and is thus unobtainable by the selected technique. Another line is plotted showing the physically feasible dislocation density measureable at each step size.

Any data below that line corresponds to a fraction of a dislocation per Burger's circuit, which is not physical. The physically feasible minimum dislocation density is given by:

$$\rho_{\min} = \frac{1}{L^2} \tag{20}$$

$\rho_{\min}$ is the dislocation density corresponding to one dislocation per Burger's circuit.

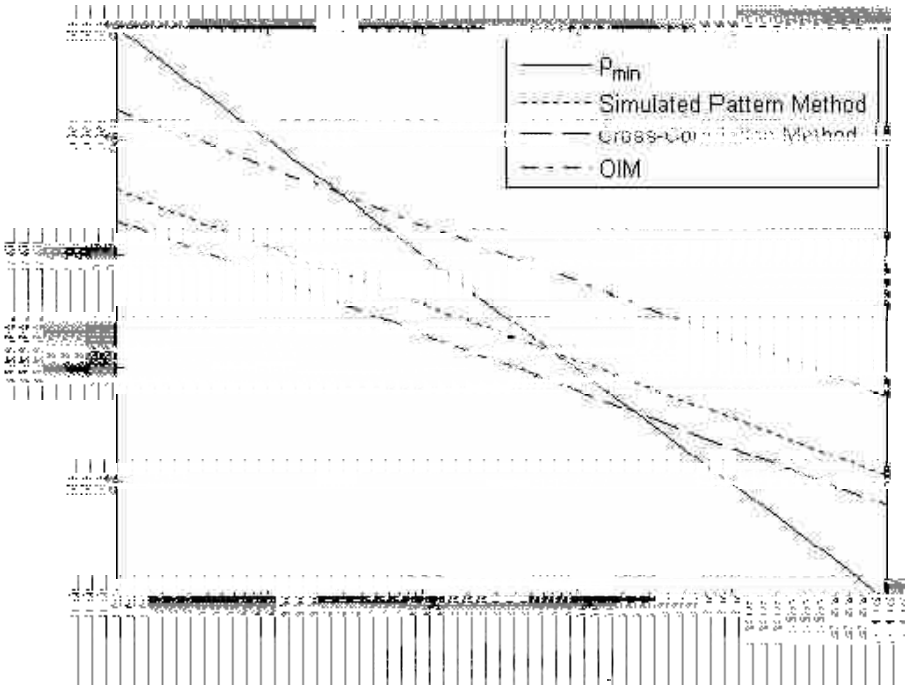

Figure 4-2: Step size considerations when estimating dislocation densities.

Average dislocation densities have been commonly measured to be ~10^{13}-10^{16} m^{-2}. Because of angular resolution limitations in OIM, a relatively large step size must be used to resolve such dislocation densities. However, this increases the risk of

many of the dislocations cancelling each other out within the Burger's circuit. By increasing the angular resolution using cross-correlation techniques, the resolution of dislocation density estimates can be improved by more than an order of magnitude over traditional OIM-based techniques.

To demonstrate the effect of angular resolution on dislocation density estimates, a number of dislocation networks in a material were simulated. The networks were simulated to have a random distribution of positive and negative dislocations and a set total dislocation density. Using these simulated networks, the dislocation density was estimated at increasing step sizes. A random noise component was added to the measured data that corresponds to the angular resolution of each technique. For comparison, a reference line was also plotted with no noise component (figure 4-3).

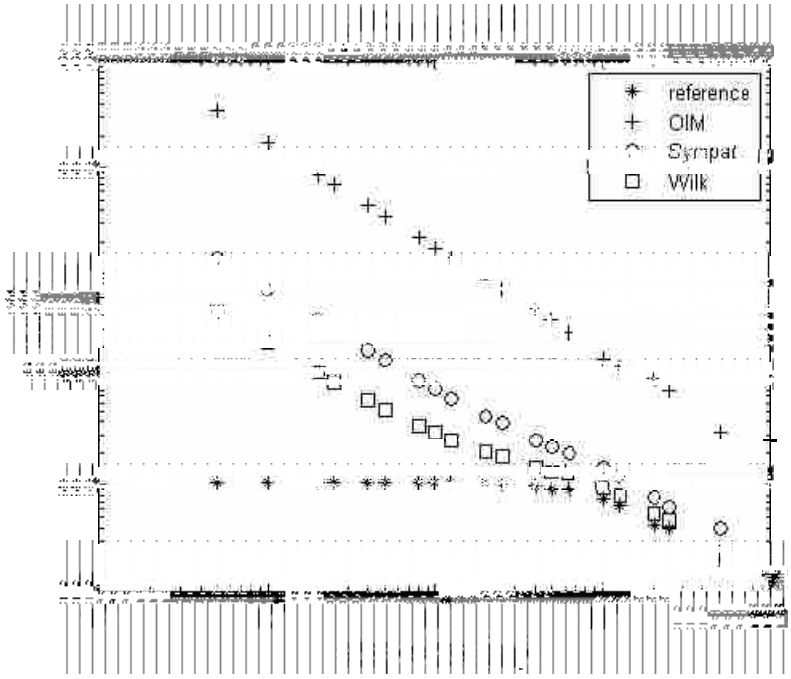

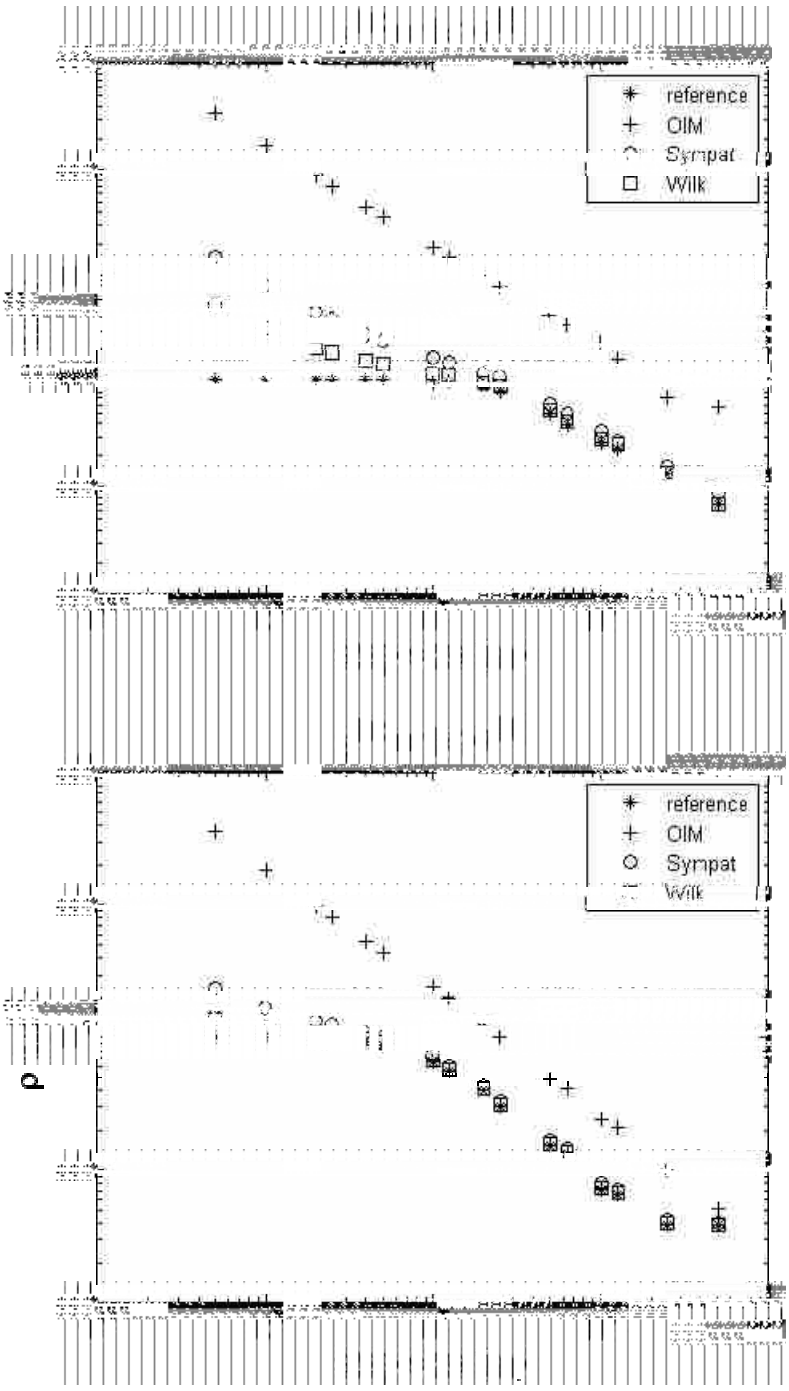
reference
OIM
Sympat
Wilk
reference
OIM
Sympat
Wilk

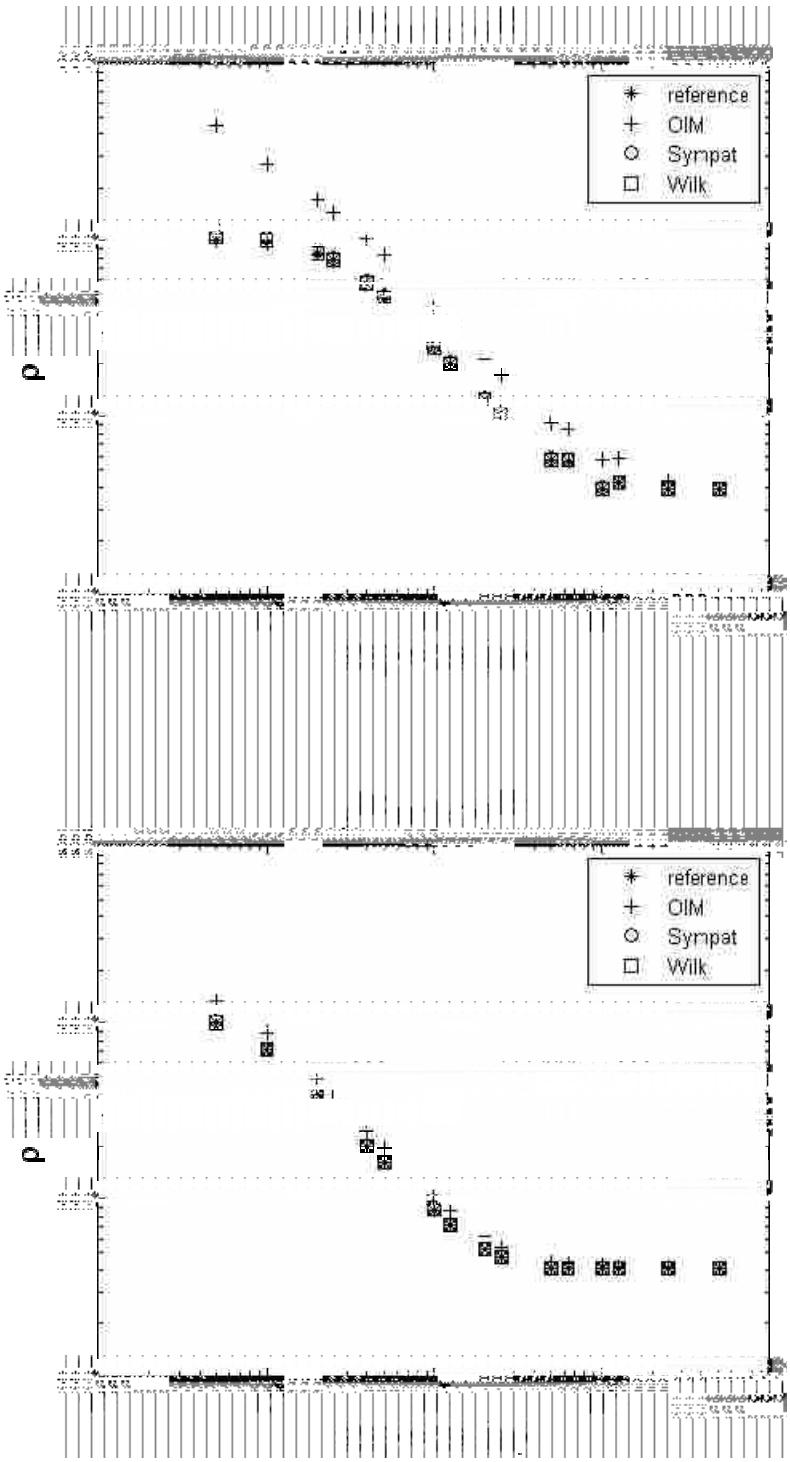

Figure 4-3: Simulated dislocation density measurements. x-axis refers to GNDs.

The following conclusions can be drawn from the simulated data. First, it can be seen that the data follows a general trend of reaching a plateau at the total dislocation density. This plateau for every case except for high dislocation densities is reached at a significantly larger step size than the minimum plotted step size. It is a common misconception that a smaller step size will always lead to more accurate data. Instead, the opposite is often the case. As the step size decreases, the noise component of the data becomes increasingly dominant, and important information is lost. Instead, the selection of the step size should be dependent on the expected dislocation density. High dislocation densities require a small step size to resolve the dislocation structure, but a larger step size should be selected when dealing with materials that have relatively low dislocation densities. There is also a plateau at the tail end of the data. This plateau corresponds to the step size at which all SSDs are averaged out, and only GNDs remain. Second, at the end of the top plateau (corresponding to the step size where every dislocation is resolved), the estimated dislocation density steadily decreases. This is due to dislocations of opposite signs cancelling each other within a Burger's circuit. So, while there is danger from noise effects in choosing too small a step size, care must also be taken so as to not choose so large a step size that important data is averaged out. Third, OIM techniques are capable of meaningful dislocation density estimates only for high dislocation densities (of the order of $\sim 10^{16}$ m^{-2}). This makes OIM useful for detecting large dislocation pileups as might be expected to occur near grain boundaries in deformed materials, but ineffective as a tool for studying more general dislocation structures. Cross-correlation methods offer over an order of magnitude improvement in angular resolution making dislocation structure characterization at high resolution much more feasible.

An added advantage of cross-correlation techniques over traditional OIM is the ability to access elastic strain data. OIM is insensitive to the elastic strain in a material, and so it is assumed to be negligible when estimating dislocation densities. Cross-correlation techniques provide the elastic strain information and allow for its inclusion in Kröner's formula.

4.2 Application to magnesium

Dislocation density measurements are an important factor in the development of new metallic materials. Due to its light weight and high recyclability, magnesium alloys are very attractive prospects for applications in car parts. However, their use is limited by low ductility and formability at low temperatures [29-32]. This low ductility is based on the limited number of slip systems that are active at room temperatures. One way to see this effect is through studying the dislocation densities caused by slip in the crystal lattice. A better understanding of the dislocation structure can lead to a more fundamental understanding of the deformation mechanisms of magnesium.

The simulated pattern method was used to estimate the dislocation density of a polycrystalline Mg AZ91 sample that had been compressed 5.5%. The normal to the sample surface was parallel to the compression direction. The sample was prepared and scanned at GM facilities in Detroit. A 4x4 μm scan was taken near the center of a 20x20 μm grain at a 100 nm step size. The scan was taken using an accelerating voltage of 20 kV and at a working distance of 12 mm. In order to obtain the highest signal-to-noise ratio possible, the EBSD patterns were saved at the full camera resolution (465x465 pixels for the camera used in this study) which slowed scanning time to ~3 patterns/sec.

To further improve the accuracy of the cross-correlations, a band pass filter was used on the overall patterns (both measured and simulated) and a low pass filter was applied to each individual ROI. The cut-off frequencies for the band pass filters (in cycles per pixel) were 0.0065 for the high pass and 0.32 for the low pass. The cut-off frequency of the low pass filter was 0.0077 cycles per pixel. These values were obtained by visual optimization to minimize the scatter in the data. The saved patterns were analyzed offline using the simulated pattern method with the OIM measured orientation as the starting point in the iterations. The offline analysis time is dependent on the number of iterations used, which is generally 3-5. For 465x465 pixel images, each iteration requires ~0.5 seconds, with two thirds of the time used for pattern simulation and the rest to perform the cross-correlation analysis. The code used has not been optimized for speed, and it is expected that the time requirements will be significantly reduced in the future.

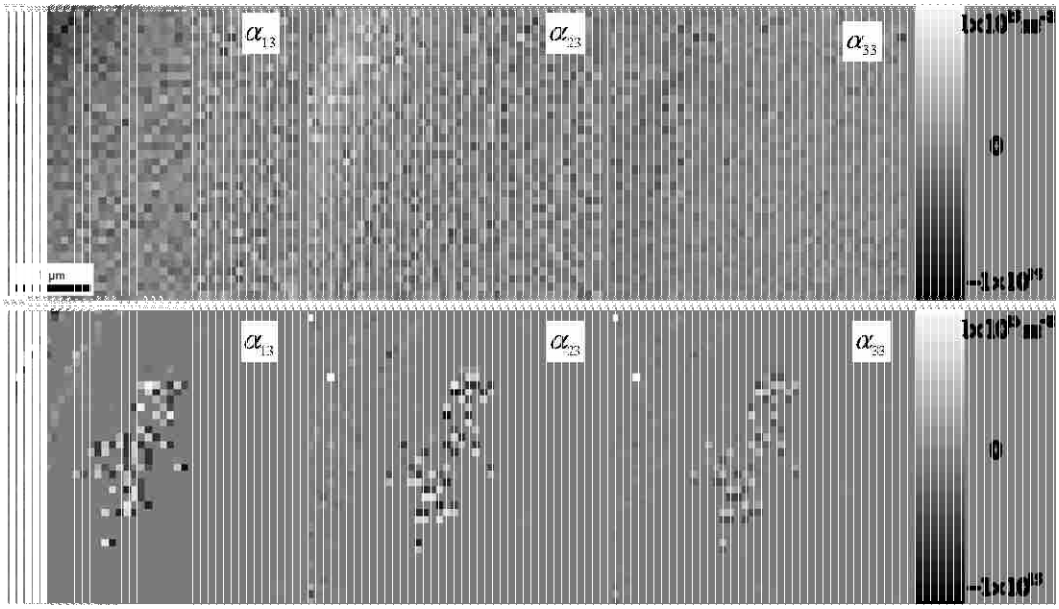

Figure 4-4: Spatial distribution of three components of the dislocation density tensor as estimated by the simulated pattern method (top row) compared to the estimation made using conventional OIM data (bottom row).

The dislocation density was first estimated using the OIM measured orientation, and then using the simulated pattern method with and without including the elastic strain term. Since dislocation density measurements need only the gradients of the elastic strain and orientation, Wilkinson's method was also used as a comparison to further validate the simulated pattern method. The dislocation density was defined as the average of the absolute magnitude of all of the points in the scan (Table 4-1).

Table 4-1: Comparison of methods for dislocation density measurements in m^{-2}

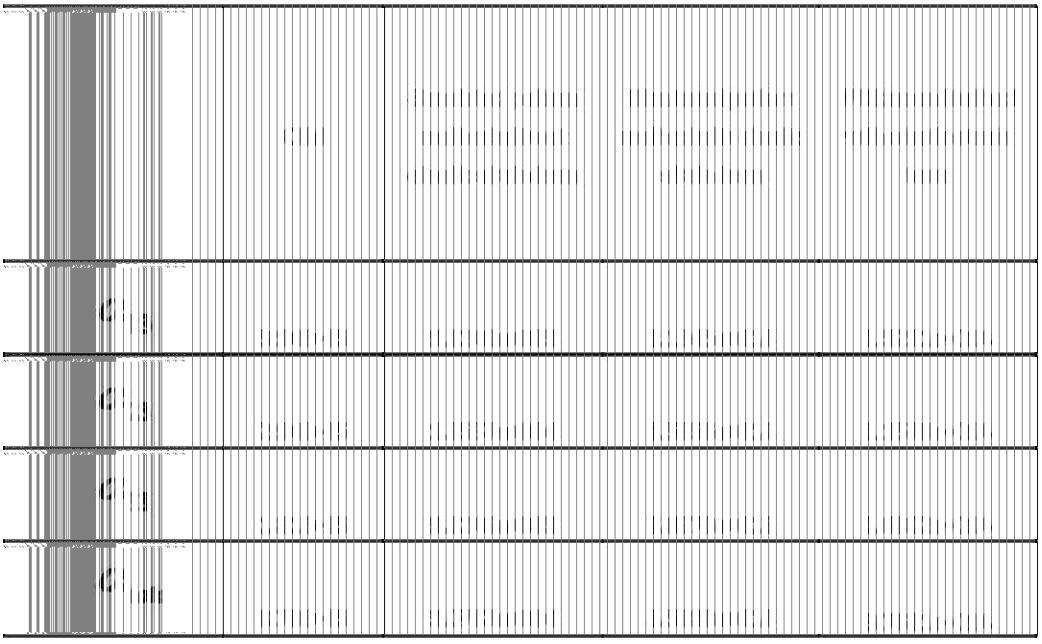

4.3 Discussion

The data obtained using Wilkinson's method were very close to that obtained using the simulated pattern method. This serves as further validation of the accuracy of the results. The OIM estimated dislocation density on the other hand was over a full order

of magnitude higher than that estimated using the simulated pattern method. In general, OIM is incapable of measuring dislocation densities below $\sim 3\times10^{15} m^{-2}$, so the estimated density in this case is around what would be expected if only noise was measured. Although no significant structure is seen in the figure, there are two important points to be taken from it. First, the dislocation density measurements using the simulated pattern method are over a full order of magnitude lower than those measured by traditional OIM. This is directly related to the increase in angular resolution of the simulated pattern method. Second, the dislocation density maps created by traditional OIM have many very high points as can be seen in the center of the scan, while other points show a very low dislocation density. These sharp changes in dislocation density are attributed to scatter in the orientation data collected by OIM and suggest that while the overall dislocation density measured by OIM may differ from the simulated pattern method by only an order of magnitude, local variations caused by scatter can cause much higher levels of error.

From the data it is also seen that the elastic strain term can have a significant effect on the estimated dislocation density. Depending on how the elastic strain aligns with the dislocations, the inclusion of the elastic strain tensor can cause a higher or lower dislocation density to be estimated. In this case, the overall estimated dislocation density increased 15% after the inclusion of the elastic strain term.

5 Tetragonality Measurements in FSW HSLA 65 Steel

5.1 Background

Steel is the most used of all metals [33-36]. It is also one of the most complicated. Different treatments and alloying contents can produce very different properties. The physics behind these processes is often poorly understood. Many of the processes developed with steel have been found through trial and error which is both costly and time consuming.

One of the most influential factors in determining the properties of steel is the carbon concentration and distribution in the iron lattice [37]. Depending on the carbon content and environmental conditions, the steel crystal lattice can either be bcc, fcc, hcp, or bc tetragonal. It is relatively simple to distinguish between fcc, bcc, and hcp lattices using existing EBSD based texture analysis methods. The characterization of tetragonalities, however, presents a more formidable challenge.

The bc tetragonal phase arises in steel lattices when carbon atoms occupy interstitial positions in the bcc iron lattice. The carbon atoms occupy the octahedral sites, causing a larger expansion along the c axis than along the a axis (figure 5-1). The

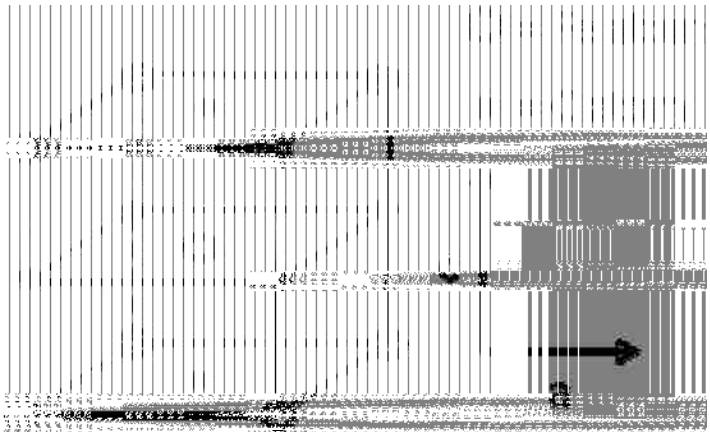

Figure 5-1: Schematic of carbon atoms occupying the octehedral sites in an iron lattice

magnitude of the tetragonality is proportional to the carbon concentration and is estimated to be [38]:

$$c/a = 1 + 0.045 wt\%C \tag{22}$$

where *wt%C* is the weight percent of carbon in the steel. The ability to measure both the magnitude and axis of this tetragonality at high resolution would provide a wealth of information on the variations in carbon concentrations and the interactions of different steel phases.

There are two steel phases in which lattice tetragonalities are found, namely the martensite and bainite phases. Martensite is formed by rapid quenching of steels with high carbon concentrations. At elevated temperatures, the austenite phase can form in steels. Austenite has an fcc iron lattice with a high concentration of interstitial carbon atoms. At room temperature, austenite becomes unstable. When steel is rapidly quenched,

the lattice structure of austenite changes with little carbon diffusion to form martensite. Since most of the carbon is retained from the austenite, the martensite phase occurs at relatively high concentrations of carbon (~0.8wt%C), causing the formation of a bc tetragonal phase [38]. Using traditional OIM, this tetragonality can usually be detected but difficulties still arise when attempting to determine the axis of tetragonality.

Bainite is more complicated than martensite and its discovery and identification occurred at a much later time. Bainite forms when steel is cooled too rapidly for pearlite to form, but not rapidly enough for martensite to form. Some carbon is still retained in the lattice, but there is still much debate in the literature on the magnitude and nature of the carbon concentrations [39]. Much of this debate is due to the lack of adequate techniques to fully understand and characterize the physics behind the bainite phase [40]. A brief review of the current techniques used to study the bainite and martensite phases is presented.

TEM offers the most direct visualization of the different phases of steel. Methods such as convergent beam electron diffraction (CBED) and high resolution TEM allow for the direct observation of the tetragonality in steel phases [41], the interaction of the different phases at interfaces [42], and the morphology of the microstructure [43]. There are, however, a few significant drawbacks of using TEM for studying steel. The need for a thin foil sample introduces two free surfaces. This can cause strain relaxation in the sample and lead to erroneous conclusions on the observed phenomena. Also, TEM is very limited in the size of the area for characterization. Only very small areas can be observed at a time, making it difficult to collect statistically significant amounts of data from samples.

X-ray spectroscopy techniques such as energy dispersive x-ray spectroscopy (EDS) have been used to find the composition of steels at discrete points in a sample [44-46]. EDS has the advantage over many other methods that it allows for the direct measurement of carbon concentration without relying on secondary data such as lattice parameters to estimate the chemical composition. Both SEMs and TEMs are routinely equipped with x-ray detectors for x-ray spectroscopy. In the SEM, EDS has been successfully coupled with OIM to simultaneously characterize the microstructure and the chemistry of a material at discrete points in an automated manner. Some significant drawbacks of EDS are that the total carbon content of the sample must be known for calibration purposes and the spatial resolution of EDS is significantly worse than EBSD.

Traditional OIM has been profitably used to study more of the physics behind steel phases. This is done in a few different ways. Different phases are simple to distinguish using OIM when each phase has a different lattice structure. For example, this is the case when distinguishing austenite (fcc lattice) from ferrite (bcc lattice). Lattice tetragonalities, if large enough, can also be directly detected using band indexing through the Hough transform. This is limited to large tetragonalities (>5%), and is unreliable when specifying the axis of tetragonality. Some researchers have utilized the image quality to characterize steel samples. Higher dislocation densities are present in certain steel phases, leading to a decrease in the image quality. Theoretically, this could be used to detect different phases in steel samples. In practice, this method has been proven to be unreliable due to the host of other factors that also affect the image quality and the difficulty in establishing an image quality threshold value for phase identification. The orientation distribution can be used to gain information on grain morphology and

estimate the local curvature/dislocation density. This information has been used especially to identify the bainite phase, which has a high dislocation density in comparison with other steel phases [46, 47]. Thus, high dislocation density areas can be linked to the distribution of the bainite phase in a material. Some uncertainty in the data arises due to the need of setting a dislocation density threshold value for phase distinction when using this method.

5.2 Simulated pattern approach to tetragonality estimates

The simulated pattern method provides a direct way to detect and measure tetragonalities in a crystal lattice and thus access important information on phase characteristics and carbon distribution in steel samples. These tetragonalities can be detected in the diagonal components of the elastic strain term when expressed in the crystal frame.

When expressing the elastic strain term in the crystal frame, the off-diagonal terms correspond to shear strains in the unit cell. The diagonal terms correspond to normal strains, or a stretch or compression of the unit cell (figure 5-2). A stretch or compression of the unit cell can arise from two different influences – an elastic strain in the material, or a chemical composition change. Strain from the latter influence is referred to as an eigenstrain. These two influences combine resulting in the total measured strain.

In order to obtain meaningful information, these two strains must be separated. Both forms of strain result in identical shifts in the Kikuchi bands of an EBSD pattern, and so are indistinguishable from each other using the simulated pattern method. This

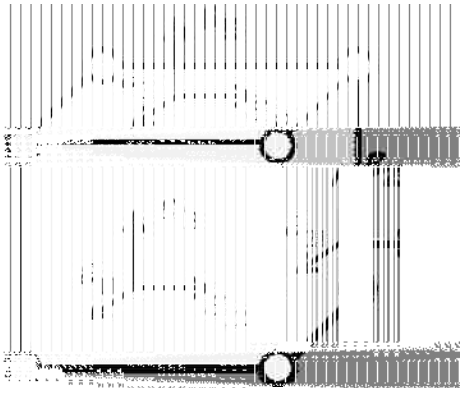

Figure 5-2: Representation of components of the elastic strain tensor.

issue is resolved when the relative magnitudes of the two different types of strain are taken into account. Plastic yielding occurs in most metallic materials at around 0.2% strain. It is expected that while local elastic strains may exceed this value, they will still be at or below 1%. Eigenstrains vary over a much larger range depending on the chemical composition of the lattice. In the case of steel samples, the tetragonality is directly related to the concentration of carbon in the lattice. This tetragonality can vary significantly from <1% to 6%. Taking this into account, measured strains above 1% can be assumed to be eigenstrains. Any values of elastic strain below 1% are inseparable using the current approach.

In the derivation of the cross-correlation method, it was shown that only the off-diagonal components of the elastic strain tensor can be measured directly. Only the difference between diagonal components of the elastic strain tensor is directly accessible using cross-correlation methods. When measuring elastic strains, the diagonal components can be separated by taking into account the free surface boundary condition. This boundary condition, however, applies to elastic strains only, not to eigenstrains. In

the case of a tetragonality from the chemical composition, the diagonal components must be separated in a different manner.

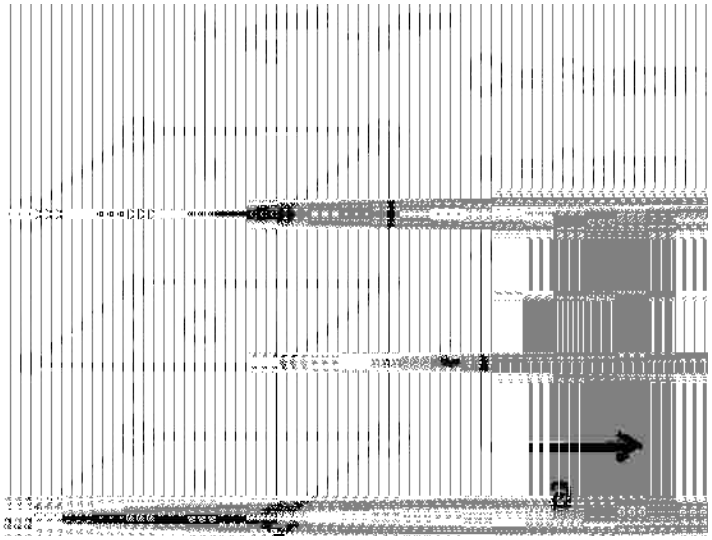

Figure 5-3: Schematic of how an eigenstrain stretches the crystal lattice.

The elastic strain tensor in a phase with a tetragonality along the $\hat{e}_3$ axis in the crystal frame has the following form (shown schematically in figure 5-3):

$$\varepsilon = \begin{bmatrix} \varepsilon_{11}^{elastic} & \varepsilon_{12}^{elastic} & \varepsilon_{13}^{elastic} \\ \varepsilon_{12}^{elastic} & \varepsilon_{22}^{elastic} & \varepsilon_{23}^{elastic} \\ \varepsilon_{13}^{elastic} & \varepsilon_{23}^{elastic} & \varepsilon_{33}^{elastic} + \varepsilon^{eigen} \end{bmatrix} \tag{23}$$

Assuming that the eigenstrain is much bigger than the elastic strains, we can rewrite the elastic strain tensor as

$$\varepsilon \cong \varepsilon^{eigen} = \begin{bmatrix} 0 & 0 & 0 \\ 0 & 0 & 0 \\ 0 & 0 & \varepsilon^{eigen} \end{bmatrix} \tag{24}$$

At this point, it is a simple matter to separate the diagonal components of the strain tensor allowing the recovery of the lattice tetragonality.

5.3 FSW results

Friction stir welding (FSW) is a solid state welding process that shows much promise for minimization of failure due to poor welding. Two sheets of metal are welded together using frictional heat to bond them. The temperature of the process remains below the melting point of the material, keeping it a solid state technique.

FSW of aluminum alloys has been already widely used especially in aeronautical applications [48, 49]. FSW of steel alloys has been more difficult due to complicating factors such as its higher melting point and increased wear on the instruments [50, 51]. Traditional welding techniques can cause large changes in the metallurgy of steel samples. These metallurgical changes can be reduced using FSW techniques since the material is not heated to its melting point. There remain significant studies to be carried out to determine the microstructural changes that still do occur from the FSW process. One especially important topic is the redistribution of carbon atoms after the welding process.

In order to demonstrate the abilities and versatility of the simulated pattern method, a series of scans was taken from the weld zone of HSLA 65 steel. The steel was

thermo-mechanically processed to reduce the grain size and increase strength. The scans were taken using the custom built SEM stage for pattern center calibration. A single crystal germanium sample was used as the reference sample for the calibration. All of the patterns were stored and analyzed using the simulated pattern method to get the strain and orientation information.

Three different types of maps are used for displaying the data. The first type of map is a standard inverse pole figure (IPF) map used to display the crystallographic orientation at each point in the scan. The second type of map is a tetragonality map. The tetragonality is defined as the eigenstrain previously discussed. Experimentally, the magnitude of this tetragonality is defined as:

$$\varepsilon^{tetr} = \varepsilon_{33}^{crystal} - \frac{\varepsilon_{11}^{crystal} + \varepsilon_{22}^{crystal}}{2} \tag{25}$$

where $\varepsilon_{33}^{crystal}$ is defined as the stretched axis in the tetragonality. The map is formed by plotting ε^{tetr} at each point in the scan. A third map generated is a dislocation density map. Due to opacity limitations of the scan, the dislocation density maps are limited to a rough estimate of the total dislocation density at each point (see chapter 4 for further discussion). The dislocation density is estimated by multiplying the sum of the magnitude of the three available components of the dislocation density tensor by three.

5.3.1 OIM comparison

Grain morphology is a standard method for identification of the bainite phase. Before doing any high resolution scans, regular OIM scans were done to visualize the grain morphology in and away from the weld area.

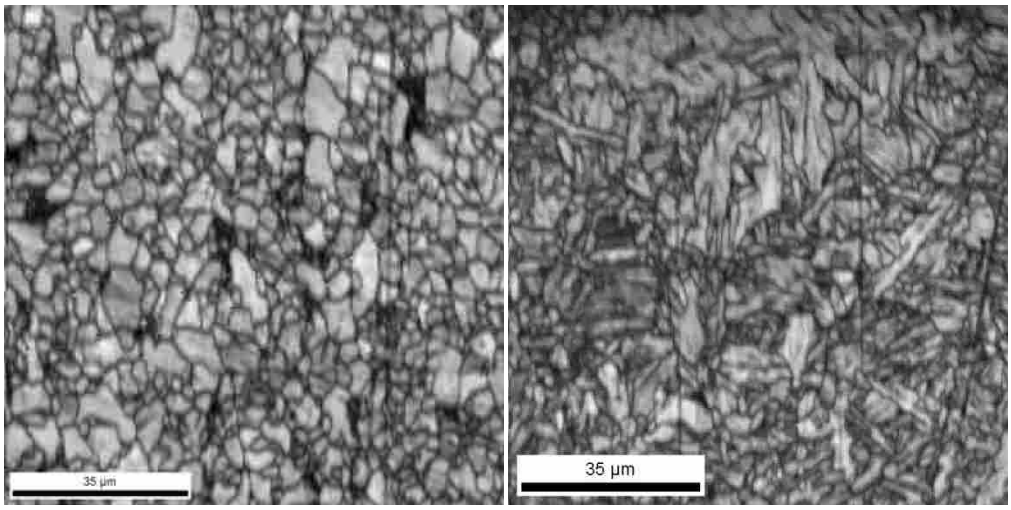

Figure 5-4: Comparison of microstructure from the undeformed lattice (left) with the microstructure of the weld area (right).

Figure 5-4 shows how the welding process affects the microstructure of the material. The polygonal grain morphology suggests that there is very little of the bainite phase in the undeformed (away from the weld) area of the sample. The lathe structure of the grains in the weld area suggests that most of the scan area is made up of the bainite phase. This can be understood by considering the heat input of the FSW process. The FSW process heats the material enough that the austenite phase forms. As the steel cools after the welding process is complete, the austenite undergoes a phase transformation into bainite [52]. There is insufficient carbon in HSLA 65 steel for martensite to form.

5.3.2 General scan conditions

All of the high resolution scans were taken with identical parameters for the simulated pattern method analysis. Each pattern was filtered using a band pass filter with an upper cutoff frequency of 0.39 cycles/pixel and a lower cutoff frequency of 0.016 cycles/pixel. Also, each individual ROI was filtered using a low pass filter with an upper cutoff frequency of 0.070 cycles/pixel. The patterns were saved at half of the camera resolution (512x512 pixels). The electron beam accelerating voltage was set to 20 kV. The acquisition time varied for each scan between 0.5-1 second per point. The long acquisition time allowed for the highest possible signal to noise ratio. The color coding for the IPF maps is given by the colored triangle (figure 5-5).

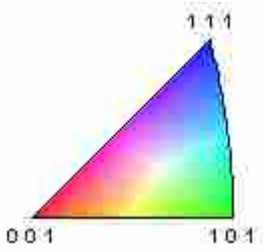

Figure 5-5: Color coding for the IPF maps.

5.3.3 Scan 1

The first high resolution scan is a 30x30 μm scan taken with a 150 nm step size. The purpose of the scan is to show the general microstructure characteristics and measured tetragonalities in the crystal lattice outside of the welded area. Also, the scan

acts as verification that the simulated pattern method does not measure large tetragonalities in areas of little carbon concentration.

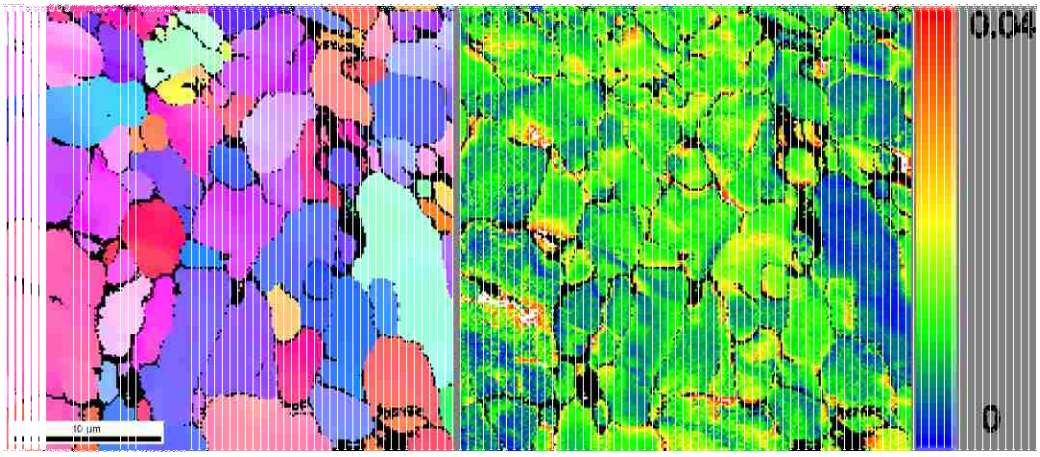

Figure 5-6: Scan 1 - IPF map (left) and tetragonality map (right) from the undeformed portion of the steel sample.

The results show that throughout the microstructure, there is very little tetragonality in any of the grains (figure 5-6). There are a few exceptions to this, especially around the grain boundaries, but for the most part the tetragonality stays around 1%. Also, the grain morphology is generally polygonal. Both of these results suggest what is expected, that there is very little carbon or bainitic steel away from the weld area. These results can be used as a reference to estimate the expected magnitude of tetragonalities in areas of little to no carbon concentration.

5.3.4 Scan 2

Scan 2 is a 100x100 µm scan taken with a 550 nm step size. The material has a very small grain size, so the scan size was sufficient to characterize many individual grains.

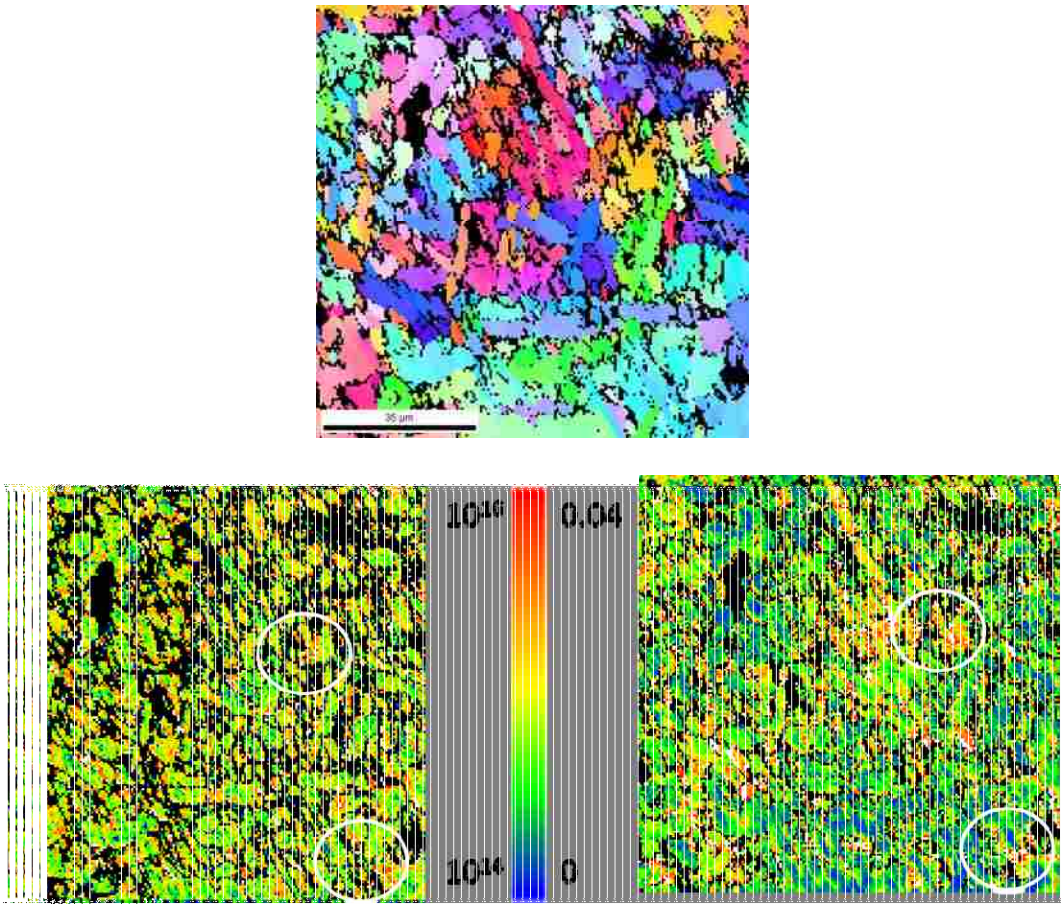

Figure 5-7: Scan 2 - IPF map (top) and comparison of a dislocation density map in m^{-2} (lower right) with a tetragonality map (lower left). White circles indicate areas of corresponding high tetragonality and high dislocation density.

All three types of maps were generated for this scan. The points that were not indexed properly are colored black. As can be observed from the IPF map (figure 5-7), this occurred primarily along the grain boundaries. There are two reasons for this to

happen. As the electron beam approaches a grain boundary, the interaction volume can straddle the boundary, and so data is collected from two different orientations. This causes overlapping EBSD patterns to be collected. When the patterns are mixed severely enough, the software is unable to distinguish between them, and they are not indexed. Also, dislocation pileups and higher carbon concentrations tend to occur near grain boundaries. Both result in the deterioration of the EBSD patterns and can lead to the patterns not being indexed.

The tetragonality map and dislocation density map were generated for comparison purposes. Careful inspection of the two maps shows that regions of high dislocation density often correspond with areas of high tetragonality. This is in agreement with current data on the bainite phase [40]. The dislocation density map provides fewer data points than the tetragonality map. This is because dislocation density estimates require at least three good points to estimate the three available components of the dislocation density tensor. Near grain boundaries, there is often an insufficient number of indexed points to estimate the dislocation density, so more of the data is inaccessible. The simulated pattern method is not reliant on neighboring points to process the information so it does not encounter the same problem.

The number if grains collected allows for the observation of the tetragonality variations at the mesoscale. In theory, this should give a good estimate of the carbon distribution as well. As can be seen from the map, lattice tetragonalities can vary significantly between grains. Since orientation information is collected along with the strain data, lattice tetragonalities can also be linked to microstructure characteristics. For

example, from scan 2 a correlation between higher tetragonality and the [0 0 1] orientation can be made.

Scan 2 highlights an important ability of the simulated pattern method. Relatively large areas of a sample can be characterized in a non-destructive way that allows for lattice tetragonality variation information. This allows for finding links between microstructure characteristics such as grain size and orientation and the local lattice tetragonality. In order to verify connections between microstructure and local lattice tetragonality, a statistically significant number of grains must be analyzed (on the order of hundreds to thousands). To analyze such a large number of grains using a TEM is extremely time consuming and labor intensive. To collect statistically significant data sets that include the local tetragonalities on an SEM is a relatively simple matter and is possible using the simulated pattern method. Scan 2 also emphasizes the advantage of using simulated patterns as reference patterns when characterizing polycrystalline materials. It is highly unlikely that a strain free reference pattern could be found in the majority of the grains in scan 2, and the limited number of points per grain makes the gradient information less reliable or useful.

5.3.5 Scan 3

Scan 3 is similar to scan 2 except it was collected at a higher spatial resolution (figure 5-8). The step size in scan 3 is 300 nm, and the total scan area is 30x30 μm. This still allows for several grains to be characterized while also providing detail on the interior structure and tetragonality variations within individual grains.

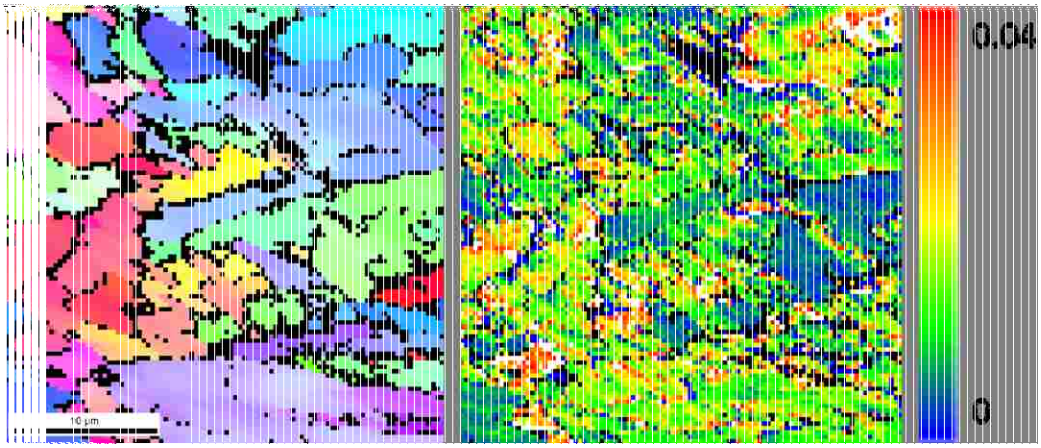

Figure 5-8: Scan 3 - IPF map (right) and tetragonality map (left).

As observed in scan 2, there appears to be more and less favorable grain orientations for high tetragonalities. With the finer step size, it is also seen that the lattice tetragonality within grains varies significantly. The magnitude of the tetragonality is especially high near the grain boundaries, although some grain boundaries appear to be much more conducive to large tetragonalities than others. This can be seen from comparing the magnitude of the tetragonality in the grain with the [1 1 1] orientation in the upper right corner to the [1 0 1] oriented grain in the middle right side.

Scan 3 highlights the ability of the simulated pattern method to capture multiple grains and still provide interesting details on the interior structure of grains.

5.3.6 Scan 4

Scan 4 was taken for correlation purposes with EDS data. Since lattice tetragonality is theoretically linked with the carbon concentration, both the EDS and tetragonality maps should display the same information. The scan size is 30x30 µm with

a step size of 500 nm. EDS data was collected simultaneously with the EBSD patterns and was then used to generate a carbon distribution map (figure 5-9).

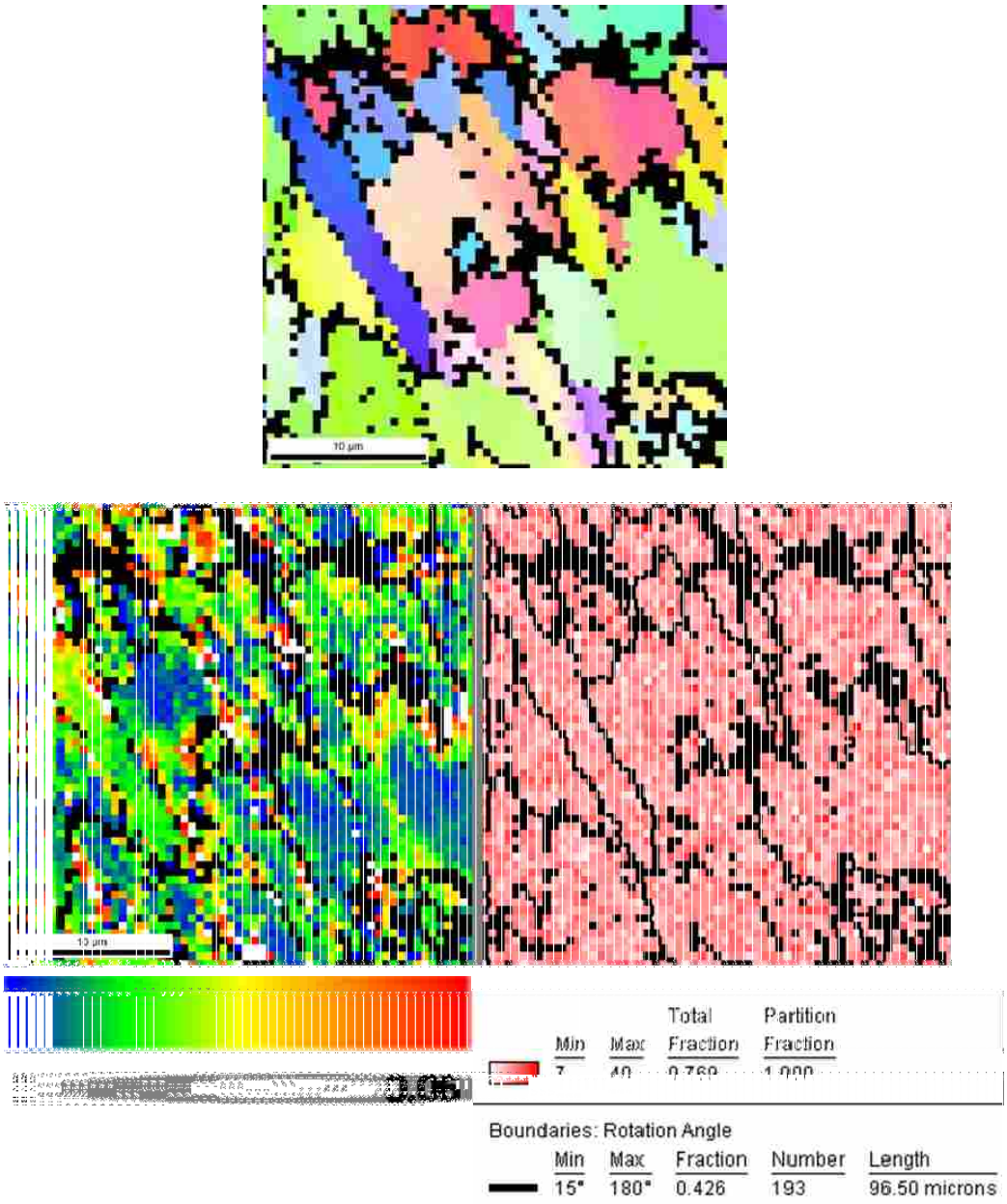

Figure 5-9: Scan 4 - IPF map (top) and comparison of tetragonality map (lower left) with EDS map of carbon distribution (lower right)

Some imagination is needed to find useful data in the carbon distribution map. This is likely due in part to the lower spatial resolution of EDS techniques in comparison with EBSD. The interaction volume from which x-rays are detected is much bigger than the interaction volume that backscattered electrons are detected from. This causes the EDS data to be averaged over a larger volume, and can lead to smearing in the data. EBSD provides a higher spatial resolution which allows for the resolution of finer details. This can be seen when comparing the carbon distribution map with the tetragonality map. Local gradients of tetragonality can be detected from the simulated pattern method analysis that are unavailable to EDS at current resolutions.

Scan 4 highlights the ability of the simulated pattern method's ability to detect fine scale features unobtainable using EDS without having to rely on more difficult and demanding techniques such as TEM.

5.3.7 Scan 5-6

Scans 5 and 6 were both taken at a much finer length scale than the other scans. The step size was chosen to be 50 nm for both scans and the full scan size was 5x5 μm for scan 5 and 5x2.15 μm for scan 6. At this length scale, much of the fine detail leading up to the grain boundaries can be observed. Overlapping pattern effects limit the data right at the grain boundaries (figure 5-10 and 5-11).

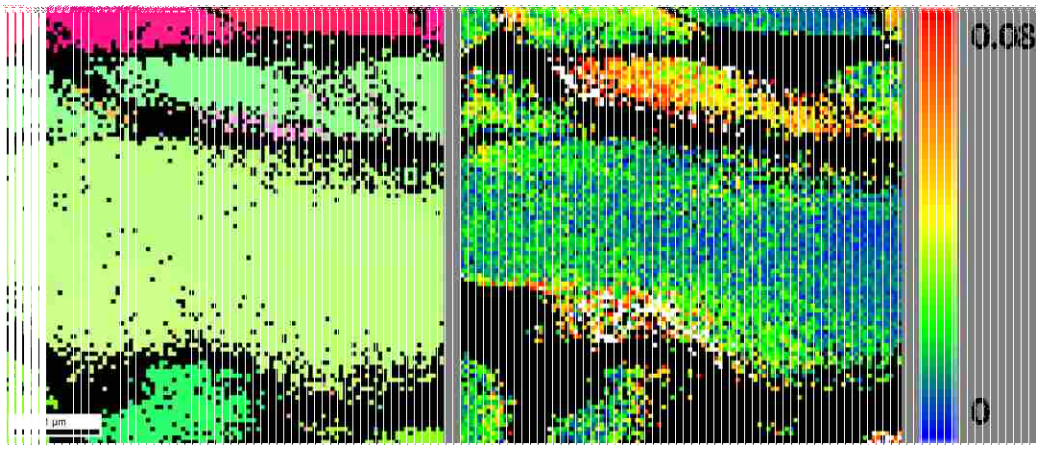

Figure 5-10: Scan 5 - IPF map (left) and tetragonality map (right).

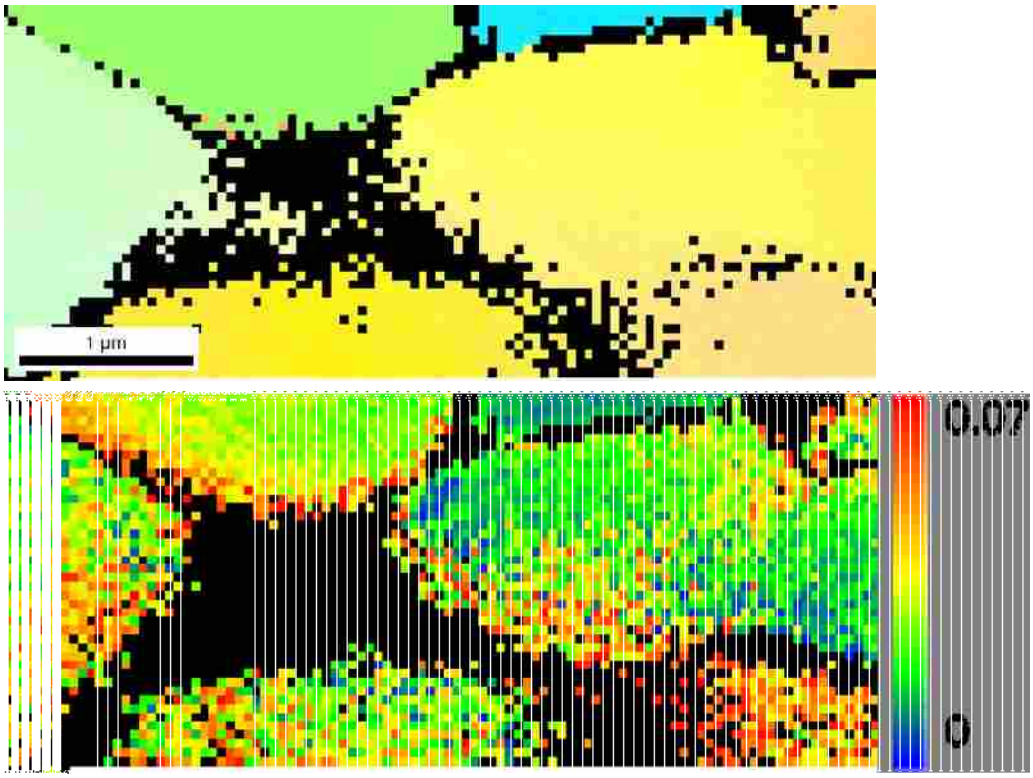

Figure 5-11: Scan 6 - IPF map (top) and tetragonality map (bottom).

It can be quickly seen that the higher tetragonalities occur near the grain boundaries for the most part. Interestingly, high tetragonalities do not occur at all of the

grain boundaries. In both scans, there are some grain boundaries, and entire grains in general, that have high tetragonalities, while others remain at relatively low tetragonalities. This is apparent when comparing the upper middle grain (low tetragonality at the grain boundary) with the lower right corner grain (high tetragonality at the grain boundary) in scan 6. Also, very fine scale gradients of the magnitude of tetragonality can be seen across the grains and near grain boundaries.

Scans 5 and 6 highlight the simulated pattern method's high resolution abilities. Previously, only TEM techniques could give such high resolution information on the tetragonalities found in the lattice parameters. The simulated pattern method offers similar information as could be obtained using TEM, but with the advantages of ease of use, ease of automation, and versatility in scan size.

5.4 Discussion

The purpose of this paper is not to go in depth on the mechanics and physics of steel processes. Instead, it is to demonstrate a powerful new method that can later lead to a more complete understanding of these processes.

The simulated pattern method offers a superior spatial resolution to dislocation density and EDS methods for phase identification and tetragonality/carbon content determination while still maintaining the ease of use that both methods provide. It also allows for large scans of many grains since it is not dependent on a strain free pattern for reference. All this is done in a nondestructive manner and with much less demanding sample preparation than is required by TEM.

The fine scale gradients of tetragonality variations within individual grains lead to much more complete information than is obtainable using other methods. There is a general trend to label and characterize each part of a steel sample so that each phase is known. While this is important in determining the properties and general characteristics of a material, it is also in many ways limiting. If instead the data is treated in a continuum sense with less strict delineation between phases, the fundamental physics of the situation can be better observed. As is often the case with new advances in techniques, changes in our understanding and labeling of materials must also undergo similar changes to reflect a more fundamental understanding of the situation.

6 Conclusions

The simulated pattern method of cross-correlation-based EBSD analysis provides high resolution elastic strain and orientation information while maintaining the ease of use that has made OIM such a valuable tool. Simulated patterns allow for a much more general application of the cross-correlation method than is possible when using a measured pattern for reference. The following conclusions can be drawn from the experiments carried out in this paper:

- The simulated pattern method has a gradient resolution limit (change in values instead of absolute values) of 0.02° for angular resolution and an elastic strain resolution of 3.6×10^{-4} for small strains and 1×10^{-3} for large strains (>0.02). This represents an order of magnitude improvement of angular resolution over OIM without any loss of applicability.
- The pattern center calibration allows for a global angular resolution limit of ~0.06°. This value does not take into account any error in the accuracy of the input sample tilt and elevation angles. The global elastic strain resolution is the same as what is stated for the gradient resolution.

Data obtained using the simulated pattern method (elastic strain and orientation information) can be used to measure and characterize a number of other properties of materials. The following have been demonstrated:

- Three components of the dislocation density tensor can be estimated using orientation and elastic strain information. The minimum resolvable dislocation density demonstrated in this paper is $1x10^{14}$ m^{-2}, although lower densities have been measured in single crystal samples. This represents an order of magnitude improvement over traditional OIM (directly proportional to the respective angular resolutions of OIM and the simulated pattern method). Additionally, the simulated pattern method takes into account the elastic strain gradient information which is inaccessible to traditional OIM. Inclusion of the elastic strain term was found to change the data by 15%.
- Lattice tetragonalities arising from compositional changes in a material, or eigenstrains, can be measured using the diagonal components of the elastic strain tensor when expressed in the crystal frame. Assuming that the elastic strains are much smaller than the eigenstrains, the minimum measurable eigenstrain is ~1%. Any eigenstrain smaller is inseparable from the elastic strains.

The applications presented in this paper are just a sampling of the many possible future applications. The simulated pattern method's versatility, ease of use, and high resolution capabilities make it a promising candidate for many more uses. There is continued work being done to improve the resolution capabilities of the simulated pattern method. This includes methods for improving the fidelity of the simulations, characterization of any optical distortions of the electron beam, and deconvolution of the interaction probe volume to increase the spatial resolution.

7 References

1. Adams, B.L., Wright, S.I., and Kunze, K., "Orientation imaging: the emergence of a new microscopy." *Metallurgical Transactions A (Physical Metallurgy and Materials Science)*, 1993. **24A**(4): p. 819-31.

2. Maitland, T.M. and Gholinia, A., "Advances in high-speed EBSD orientation mapping." *Microsc Microanal*, 2007. **13**: p. 924-925.

3. Field, D.P., "Improving the spatial resolution of EBSD." *Microsc Microanal*, 2005. **11**: p. 52-53.

4. Ren, S.X., et al., "Exploring spatial resolution in electron back-scattered diffraction experiments via monte carlo simulation." *Microsc Microanal*, 1998. **4**: p. 15-22.

5. Humphreys, F.J., "Characterisation of fine-scale microstructures by electron backscatter diffraction (EBSD)." *Scripta Materialia*, 2004. **51**: p. 771-776.

6. Tao, X. and Eades, A., "Monte Carlo Simulation for Electron Backscattering Diffraction." *Microsc Microanal*, 2004. **10**(2): p. 940-941.

7. Zaefferer, S., Wright, S.I., and Raabe, D., "3D-orientation microscopy in a FIB SEM: a new dimension of microstructure characterisation." *Microsc Microanal*, 2007. **13**: p. 1508-1509.

8. de Kloe, R., Shulz, H., and Reinauer, F., "Advances in 3-dimensional material characterisation using simultaneous EDS and EBSD analysis in a combined FIB-SEM microscope." *EMC*, 2008. **1**: p. 675-676.

9. Wright, S.I., "Review of automated orientation imaging microscopy (OIM)." *Journal of Computer-Assisted Microscopy*, 1993. **5**(207).

10. Troost, K.Z., Van der Sluis, P., and Gravesteijn, D.J., "Elastic strain determination by backscatter Kikuchi diffraction in the scanning electron microscope." *Applied Physics Letters*, 1993. **62**(10): p. 1110-1112.

11. Wilkinson, A.J., Meaden, G., and Dingley, D.J., "High resolution mapping of strains and rotations using electron back scatter diffraction." *Materials Science and Technology*, 2006. **22**(11): p. 1-11.

12. Wilkinson, A.J., Meaden, G., and Dingley, D.J., "High-resolution elastic strain measurement from electron backscatter diffraction patterns: New levels of sensitivity." *Ultramicroscopy*, 2006. **106**: p. 307-313.

13. Wilkinson, A.J., "High resolution measurements of strain and tilt distributions in SiGe mesas using electron backscatter diffraction." *Applied Physics Letters*, 2006. **89**(241910): p. 1-3.

14. Wilkinson, A.J., Meaden, G., and Dingley, D.J., "Elastic Strain Tensor Mapping - extending the limits of EBSD analysis." *Microsc Microanal*, 2005. **11**: p. 520-521.

15. Villert, S., et al., "Accuracy assessment of elastic strain measurement by EBSD." *Journal of Microscopy*, 2008. **233**(2): p. 290-301.

16. Landon, C., Adams, B., and Kacher, J., "High resolution methods for characterizing mesoscale dislocation structures." *Journal of Engineering Materials and Technology*, 2008. **130**(2): p. 40-45.

17. Miyamoto, G., et al., "Precise measurement of strain accommodation in austenite matrix surrounding martensite in ferrous alloys by electron backscatter diffraction analysis." *Acta Materialia*, 2009. **57**: p. 1120-1131.

18. Kacher, J., et al., "Bragg's law diffraction simulations for electron backscatter diffraction analysis." *Ultramicroscopy*, 2009.

19. Winkelmann, A., "Simulation of electron backscatter diffraction patterns." *Microc Microanal*, 2007. **13**: p. 930-931.

20. Winkelmann, A., et al., "Many-beam dynamical simulation of electron backscatter diffraction patterns." *Ultramicroscopy*, 2007. **107**: p. 414-421.

21. Zaefferer, S., "Some ideas on the formation mechanisms and intensity distribution of backscatter Kikuchi patterns." *Microc Microanal*, 2007. **13**: p. 928-929.

22. Spencer, A.J.M., *Continuum Mechanics*. 1980, New York: Longman.
23. Lagarias, J.C., et al., "Convergence properties of the Nelder-Mead simplex method in low dimensions." *SIAM J. Optim.*, 1998. **9**(1): p. 112-1147.

24. Nye, J.F., "Some geometrical relations in dislocated crystals." *Acta Metallurgica*, 1953. **1**: p. 153-162.

25. Kroner, E., "Continuum theory of dislocations and self-stresses." *Ergebnisse der Angewandten Mathematik*, 1958. **5**: p. 1327-1347.

26. Sun, S., Adams, B.L., and King, W.E., "Observations of lattice curvature near the interface of a deformed aluminium bicrystal." *Philosophical Magazine A: Physics of Condensed Matter, Structure, Defects and Mechanical Properties*, 2000. **80**(1): p. 9-25.

27. Pantleon, W., "Resolving the goemetrically necessary dislocation content by conventional electron backscattering diffraction." *Scripta Materialia*, 2008. **58**: p. 994-997.

28. Field, D.P., Merriman, C.C., and Smith, J.M., "Excess dislocation density measurement dependence on EBSD step size." *Microsc Microanal*, 2007. **13**: p. 920-921.

29. Agnew, S.R., et al., "Study of slip mechanisms in a magnesium alloy by neutron diffraction and modeling." *Scripta Materialia*, 2003. **48**: p. 1003-1008.

30. Graff, S., Brocks, W., and Steglich, D., "Yielding of magnesium: From single crystal to polycrystalline aggregates." *International Journal of Plasticity*, 2007. **23**: p. 2007.

31. Koike, J., et al., "The activity of non-basal slip systems and dynamic recovery at room temperature in fine-grained AZ31B magnesium alloys." *Acta Materialia*, 2003. **51**: p. 2055-2065.

32. Yang, P., et al., "Analysis of deformation processes of magnesium alloy at elevated temperatures by orientation mapping." *Image Anal Stereol*, 2004. **23**: p. 53-61.

33. Bhadeshia, H.K.D.H., "High Performance Bainitic Steels." *Materials Science Forum*, 2005(500): p. 63-74.

34. Caballero, F.G., et al., "Design of novel high strength bainitic steels: Part 1." *Materials Science and Technology*, 2001. **17**(512-516).

35. Takahashi, M., "Recent progress: kinetics of the bainite transformation in steels." *Current Opinion in Solid State and Materials Science*, 2004. **8**: p. 213-217.

36. Takahashi, M. and Bhadeshia, H.K.D.H., "A model for the microsctructure of some advanced bainitic steels." *MAterials Transactions, JIM*, 1991. **32**(8): p. 689-696.

37. Abreu, H.F.G.d., et al., "Deformation Induced Martensite in an AISI 301LN Stainless Steel: Characterization and Influence on Pitting Corrosion Resistance." *Materials Research*, 2007. **10**(4): p. 359-366.

38. Honeycombe, R.W.K., *Steels*. Matellurgy and Materials Science, ed. R.W.K. Honeycombe and P. Hancock. 1981, London: Edward Arnold.
39. Hase, K., Garcia-Mateo, C., and Bhadeshia, H.K.D.H., "Bainite formation influenced by large stress." *Materials Science and Technology*, 2004. **20**: p. 1499-1505.

40. Bhadeshia, H.K.D.H., *Bainite in Steels*. 1992, London: The Institute of Materials.
41. Zhang, M.X. and Kelly, P.M., "Determination of carbon content in bainitic ferrite and carbon distribution in austenite by using CBKLDP." *Materials Characterization*, 2997. **40**(3): p. 159-168.

42. Chang, L.C. and Bhadeshia, H.K.D.H., "Austenite films in bainitic microstructures." *Materials Science and Technology*, 1995. **11**: p. 874-883.

43. Yang, H.S. and Bhadeshia, H.K.D.H., "Designing low carbon, low temperature bainite." *Materials Science and Technology*, 2008. **24**(3): p. 335-342.

44. Makinson, J.D., et al., "Diffracting particle size analysis of martensite - retained austenite microstructures." *International Centre for Diffraction Data*, 2000. **43**: p. 326-341.

45. Zaefferer, S. and Romano, P., "Attempt to identify and quantify microstructural constituents in low-alloyed TRIP steels by simultaneous EBSD and EDS measurements." *Microc Microanal*, 2007. **13**: p. 944-945.

46. Zaefferer, S., Romano, P., and Friedel, F., "EBSD as a tool to identify and quantify bainite and ferrite in low-alloyed Al-TRIP steels." *Journal of Microscopy*, 2008. **3**: p. 499-508.

47. Cabus, C., Regle, H., and Bacroix, B., "Orientation relationship between ausenite and bainite in a multiphased steel." *Materials Characterization*, 2007. **58**: p. 332-338.

48. Sutton, M.A., et al., "Microstructural studies of friction stir welds in 2024-T3 aluminum." *Materials Science and Engineering A*, 2002. **323**(1-2): p. 160-166.

49. Mendez, P.F. *New trends in welding in the aeronautic industry*. in *New Trends for the Manufacturing in the Aeronautic Industry*. 2000. San Sebastian, Spain.
50. Mishra, R.S. and Ma, Z.Y., "Friction stir welding and processing." *Materials Science and Engineering R*, 2005. **50**: p. 1-78.

51. Lienert, T.J., et al., "Friction stir welding studies on mild steel." *The Welding Journal*, 2003. **Supplement**: p. 1-9.

52. Matsuda, H. and Bhadeshia, H.K.D.H., "Kinetics of the bainite transformation." *Proc. R. Soc. Lond. A*, 2004. **460**: p. 1707-1722.